Authigenic 10Be/9Be ratio signatures of the cosmogenic nuclide production linked to geomagnetic dipole moment variation since the Brunhes/Matuyama boundary

Quentin Simon, Nicolas Thouveny, Didier L Bourlès, Jean-Pierre Valet, Franck Bassinot, Luc L Ménabréaz, Valéry Guillou, Sandrine Choy, Luc L Beaufort

AGU PUBLICATIONS

JGR

Journal of Geophysical Research: Solid Earth

RESEARCH ARTICLE
10.1002/2016JB013335

Key Points:
- Authigenic $^{10}Be/^{9}Be$ ratios from three equatorial ocean cores are stacked and averaged outlining atmospheric ^{10}Be production changes
- The ^{10}Be cosmogenic nuclide overproduction episodes are systematically associated with geomagnetic dipole lows over the last 850 ka
- The ^{10}Be signatures of the Brunhes/Matuyama transition and Brunhes geomagnetic excursions yield distinct rates and durations

Supporting Information:
- Supporting Information S1
- Tables S1 to S7
- Data Set S1

Correspondence to:
Q. Simon,
simon@cerege.fr

Citation:
Simon, Q., N. Thouveny, D. L. Bourlès, J.-P. Valet, F. Bassinot, L. Ménabréaz, V. Guillou, S. Choy, and L. Beaufort (2016), Authigenic $^{10}Be/^{9}Be$ ratio signatures of the cosmogenic nuclide production linked to geomagnetic dipole moment variation since the Brunhes/Matuyama boundary, *J. Geophys. Res. Solid Earth*, *121*, doi:10.1002/2016JB013335.

Received 5 JUL 2016
Accepted 20 OCT 2016
Accepted article online 21 OCT 2016

Authigenic $^{10}Be/^{9}Be$ ratio signatures of the cosmogenic nuclide production linked to geomagnetic dipole moment variation since the Brunhes/Matuyama boundary

Quentin Simon[1,2], Nicolas Thouveny[1], Didier L. Bourlès[1], Jean-Pierre Valet[2], Franck Bassinot[3], Lucie Ménabréaz[1], Valéry Guillou[1], Sandrine Choy[1,2], and Luc Beaufort[1]

[1]CEREGE UM34, Aix-Marseille Université, CNRS, IRD, Collège de France, Aix-en-Provence, France, [2]IPGP, Sorbonne Paris-Cité, Université Paris Diderot, UMR 7154, CNRS, Paris, France, [3]LSCE, UMR 8212, LSCE/IPSL, CEA-CNRS-UVSQ and Université Paris-Saclay, Paris, France

Abstract Geomagnetic dipole moment variations associated with polarity reversals and excursions are expressed by large changes of the cosmogenic nuclide beryllium-10 (^{10}Be) production rates. Authigenic $^{10}Be/^{9}Be$ ratios (proxy of atmospheric ^{10}Be production) from oceanic cores therefore complete the classical information derived from relative paleointensity (RPI) records. This study presents new authigenic $^{10}Be/^{9}Be$ ratio results obtained from cores MD05-2920 and MD05-2930 collected in the west equatorial Pacific Ocean. Be ratios from cores MD05-2920, MD05-2930 and MD90-0961 have been stacked and averaged. Variations of the authigenic $^{10}Be/^{9}Be$ ratio are analyzed and compared with the geomagnetic dipole low series reported from global RPI stacks. The largest ^{10}Be overproduction episodes are related to dipole field collapses (below a threshold of 2×10^{22} Am^2) associated with the Brunhes/Matuyama reversal, the Laschamp (41 ka) excursion, and the Iceland Basin event (190 ka). Other significant ^{10}Be production peaks are correlated to geomagnetic excursions reported in literature. The record was then calibrated by using absolute dipole moment values drawn from the Geomagia and Pint paleointensity value databases. The ^{10}Be-derived geomagnetic dipole moment record, independent from sedimentary paleomagnetic data, covers the Brunhes-Matuyama transition and the whole Brunhes Chron. It provides new and complementary data on the amplitude and timing of millennial-scale geomagnetic dipole moment variations and particularly on dipole moment collapses triggering polarity instabilities.

1. Introduction

Knowledge of past geomagnetic dipole moment (GDM) variation is required to understand the past and present geodynamo regimes and anticipate future changes. Namely, the amplitudes and timing of these variations are the keys for understanding the underlying physical processes of dipole field instabilities [*Hulot et al.*, 2010]. Paleomagnetic investigations of sediments and lavas provide information on past variations of the dipole field [e.g., *Tauxe*, 1993; *Valet*, 2003], and it is nowadays generally accepted that polarity reversals and excursions are associated with dipole field wanings [e.g., *Laj and Channell*, 2015; *Valet and Fournier*, 2016]. These studies yield continuous records of the relative paleointensity (RPI) that are stacked and averaged to produce global RPI records. The latter can be calibrated by using absolute paleointensities from lava-flow records and transformed into virtual axial dipole moment (VADM) records. However, depositional and post-depositional remanent magnetization (DRM and pDRM) acquisition processes in sediments may introduce biases, hampering accurate geomagnetic interpretations [e.g., *Tauxe et al.*, 2006; *Roberts et al.*, 2013; *Valet and Fournier*, 2016]. Some discrepancies linked to such environmental biases are partially resolved by stacking and averaging individual records [e.g., *Guyodo and Valet*, 1996, 1999; *Laj et al.*, 2000, 2004; *Stoner et al.*, 2002; *Thouveny et al.*, 2004; *Yamazaki and Oda*, 2002; *Valet et al.*, 2005; *Channell et al.*, 2009; *Ziegler et al.*, 2011]. These regional and/or global RPI stacks document millennial- to million-year-scale dipole moment variations and are widely used for correlation and establishment of chronologies. However, smoothing effects inherent to stacking as well as potential distortions due to magnetization acquisition (smoothing and delays) cast doubt about time series analyses performed to extract frequencies of long-term geomagnetic variations. For these reasons few teams of geophysicists and geochemists have initiated studies of cosmogenic isotopes over geological archives in order to provide complementary data sets on variations of the geomagnetic moment.

The cosmogenic nuclide beryllium-10 (^{10}Be) production in the stratosphere (~65%) and troposphere (~35%) is triggered by spallation reactions between highly energetic primary (mainly protons (H^+) and alpha particles ($^4He^{2+}$)) and secondary (mainly neutrons) galactic cosmic ray particles and atmospheric nitrogen and oxygen atoms [*Lal and Peters*, 1967; *Dunai and Lifton*, 2014]. The penetration rate of the primary galactic cosmic ray particles into the atmosphere varies strongly with latitude as a function of the vertical cutoff rigidity, which quantifies the ability of charged particles to penetrate the geomagnetic field lines. Thus, increased ^{10}Be production results from the deficient magnetospheric shielding due to weak GDM strength. Given a nearly constant galactic cosmic ray intensity assumption [*Vogt et al.*, 1990], the factors modulating the flux of incoming primary cosmic ray particles, and then the production of cosmogenic nuclide ^{10}Be, are directly related to solar activity and Earth magnetic field variability. Previous studies have demonstrated that—while solar activity inflects the production rate on short (decadal to centennial) timescales—^{10}Be flux measured along ice and marine sediment sequences reflects large-amplitude variations of the geomagnetic dipole moment at the millennial scale [e.g., *Raisbeck et al.*, 1981; *Yiou et al.*, 1985; *Frank et al.*, 1997; *Wagner et al.*, 2000; *Carcaillet et al.*, 2004b; *Muscheler et al.*, 2005; *Ménabréaz et al.*, 2012, 2014]. After its production, the reactive $^{10}Be^{2+}$ is quickly removed from the atmosphere, i.e., 1–3 years [*Raisbeck et al.*, 1981; *Beer et al.*, 1990; *Baroni et al.*, 2011], and rapidly scavenged from the water column with typical residence time of ~100 years at ocean margins [*Anderson et al.*, 1990]. Recent studies on marine and glacial records together with simulation using general circulation models provide conclusive arguments for a rapid global atmospheric mixing of ^{10}Be before deposition [*Ménabréaz et al.*, 2012; *Heikkilä et al.*, 2009, 2013]. Altogether, the ^{10}Be time response is significantly more rapid than GDM millennial-scale fluctuations supporting the use of ^{10}Be to estimate precise GDM timing.

The inverse relationship between the geomagnetic dipole moment and the atmospheric production rate of ^{10}Be was first established by *Elsasser et al.* [1956] and progressively improved [*Lal*, 1988; *Beer et al.*, 1990; *Masarik and Beer*, 1999, 2009; *Kovaltsov and Usoskin*, 2010]. It provides the approach, independent from paleomagnetism, to decipher past GDM variations from marine sedimentary sequences from which paleomagnetic information can also be extracted [e.g., *Carcaillet et al.*, 2003, 2004b].

In this study, we present new authigenic ^{10}Be/^{9}Be ratio results obtained from cores MD05-2920 (covering the time interval 20–386 ka) and MD05-2930 (5–250 ka) collected in the west equatorial Pacific Ocean. These data are merged with a revised data set from cores MD05-2930 (250–790 ka) [*Ménabréaz et al.*, 2014] and MD90-0961 (686–873 ka) [*Valet et al.*, 2014]. The resulting stacked and averaged record provides the first nearly continuous sedimentary record of ^{10}Be production rate covering the Brunhes Chron.

2. Materials and Methods

2.1. Core Description and Environmental Settings

Cores MD05-2920 and MD05-2930 were collected by using the giant piston corer CALYPSO during the MD-148 PECTEN IMAGES XIII Cruise aboard the R/V *Marion Dufresne* in 2005 [*Beaufort et al.*, 2005]. The core site MD05-2920 (2.51°S, 144.32°E; 1848 m water depth) is located on the north coast of Papua New Guinea in the Bismarck Sea, at 100 km off the Sepik and Ramu river estuaries (Figure 1). The MD05-2920 sequence is 36.7 m long and mainly composed of homogeneous grayish olive clays with dispersed bioclasts and foraminiferal tests. The two major components of the sediments are terrigenous clays and pelagic carbonates. The sedimentary elemental composition determined by X-ray fluorescence analyses does not present any clear glacial-interglacial variability, which suggests that glacial/interglacial alternation exerted a limited influence on the regional hydrological cycle that drives the main sedimentological changes in the region [*Tachikawa et al.*, 2011, 2014]. The core site MD05-2930 (10°32′S, 146°73′E; 1490 m water depth) is located in the Gulf of Papua (GOP) on a topographic high, protected from the influence of gravity flows from the Papua shelf (Figure 1). The 36.9 m long core consists mainly of homogenous gray-green clayey and silty-clayey muds rich in foraminifera. The core is composed of dominant siliciclastic fraction fed by major rivers that drain the southern Papua New Guinea Island and by less than 40% detrital carbonates coming mainly from the northern extension of the Great Barrier Reef [*Beaufort et al.*, 2005; *McFadden et al.*, 2006]. The GOP sedimentation has been largely influenced by sea level fluctuations during the last glacial-interglacial cycles due to its proximity to the large and shallow continental margin between Australia and Papua New Guinea [*Jorry et al.*, 2008]. We also used data from core MD90-0961, collected during the SEYMAMA campaign

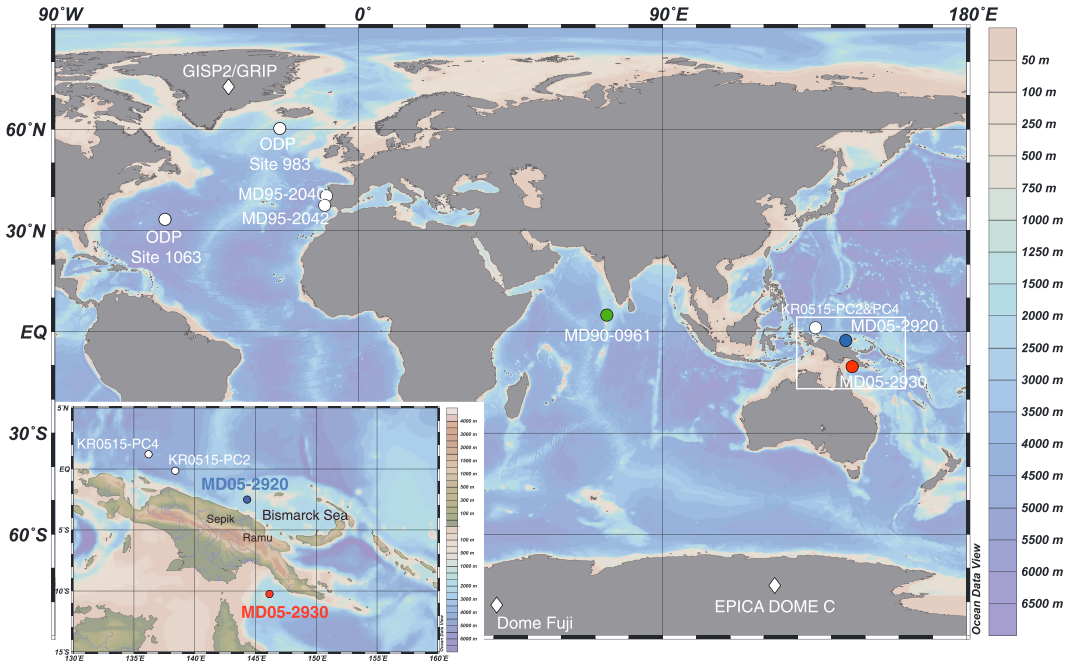

Figure 1. Site locations. Location of the three studied cores (colored circles) along with authigenic $^{10}Be/^{9}Be$ ratio and ^{10}Be flux from marine and glacial records discuss in the text. These references include Greenland Summit [*Muscheler et al.*, 2005], EPICA Dome C (EDC) [*Raisbeck et al.*, 2006; *Cauquoin et al.*, 2015], ODP Sites 983 and 1063 [*Knudsen et al.*, 2008; *Christl et al.*, 2010], Portuguese margin [*Carcaillet et al.*, 2004b; *Ménabréaz et al.*, 2011], KR0515-PC2 and KR0515-PC4, and Dome Fuji [*Horiuchi et al.*, 2016]. Results from core MD90-0961 (green) [*Valet et al.*, 2014] are included with our new results from cores MD05-2920 (blue) (Bismarck Sea) and MD05-2930 (red) (Gulf of Papua) to construct the authigenic $^{10}Be/^{9}Be$ ratio stack.

of the R/V *Marion Dufresne* in 1990. The coring site is located in the Indian Ocean, east of the Maldives platform (05°03.71°N, 73°52.57°E; 2446 m water depth; Figure 1). The lithology of this 45.7 m long core is dominated by calcareous nanofossil ooze with abundant foraminifers and clayey muds [*Valet et al.*, 2014].

2.2. Chronostratigraphic Framework

The original chronologies of the MD05-2920 and MD05-2930 sedimentary sequences [*Tachikawa et al.*, 2011; *Ménabréaz et al.*, 2014] were obtained by radiocarbon dating and by correlating their oxygen isotope ($\delta^{18}O$) records with the LR04 reference benthic stack [*Lisiecki and Raymo*, 2005]. Benthic foraminifera, *Cibicidoides wuellerstorfi* and *Uvigerina peregrina*, were picked from the 250–355 mm size fraction, at 10 or 20 cm intervals in core MD05-2920 [*Tachikawa et al.*, 2011, 2014], and at 20 cm intervals in core MD05-2930 [*Ménabréaz et al.*, 2014]. The benthic foraminifera $\delta^{18}O$ records display clear variations, which were tuned to glacial-interglacial cycles from the LR04 [*Tachikawa et al.*, 2014; *Ménabréaz et al.*, 2014]. In this paper, we used the radiocarbon calibrations provided by *Regoli et al.* [2015] for core MD05-2930, and we recalibrate ^{14}C ages in core MD05-2920 by using the Marine13 calibration curve [*Reimer et al.*, 2013] (see Tables S1 and S2 in the supporting information). We improved the resolution of original chronologies by adding, and slightly shifting, several tie points from both cores to increase their correlation with the reference LR04 stack (Figure 2). The age uncertainties resulting from the alignments of $\delta^{18}O$ records with LR04 is assumed at ± 4 ka [*Lisiecki and Raymo*, 2005]. Moreover, we set the authigenic $^{10}Be/^{9}Be$ ratio peak corresponding to the well-recognized Laschamp excursion to 41.3 ± 0.6 ka B.P. [*Laj et al.*, 2014] in order to improve our time resolution within the marine oxygen isotope stage (MIS) 3 interval. That age corresponds to the Laschamp age from the GICC05 age model of Greenland ice cores, i.e., 41.2 ± 1.6 ka B.P. [*Svensson et al.*, 2008] further supporting its reliability. This is the only firm tie point directly derived from the authigenic $^{10}Be/^{9}Be$ ratio records as we want to avoid any chronological application of the cosmogenic records in this study. Note that the comparison of records combining high-resolution $\delta^{18}O$ and authigenic $^{10}Be/^{9}Be$ ratio might be very useful to improve global correlations and evaluate regional offsets between benthic records, but this is beyond the scope of this paper. Core MD05-2920 spans the 2–11 MIS interval (20 to 386 ka), while core MD05-2930 extends to MIS

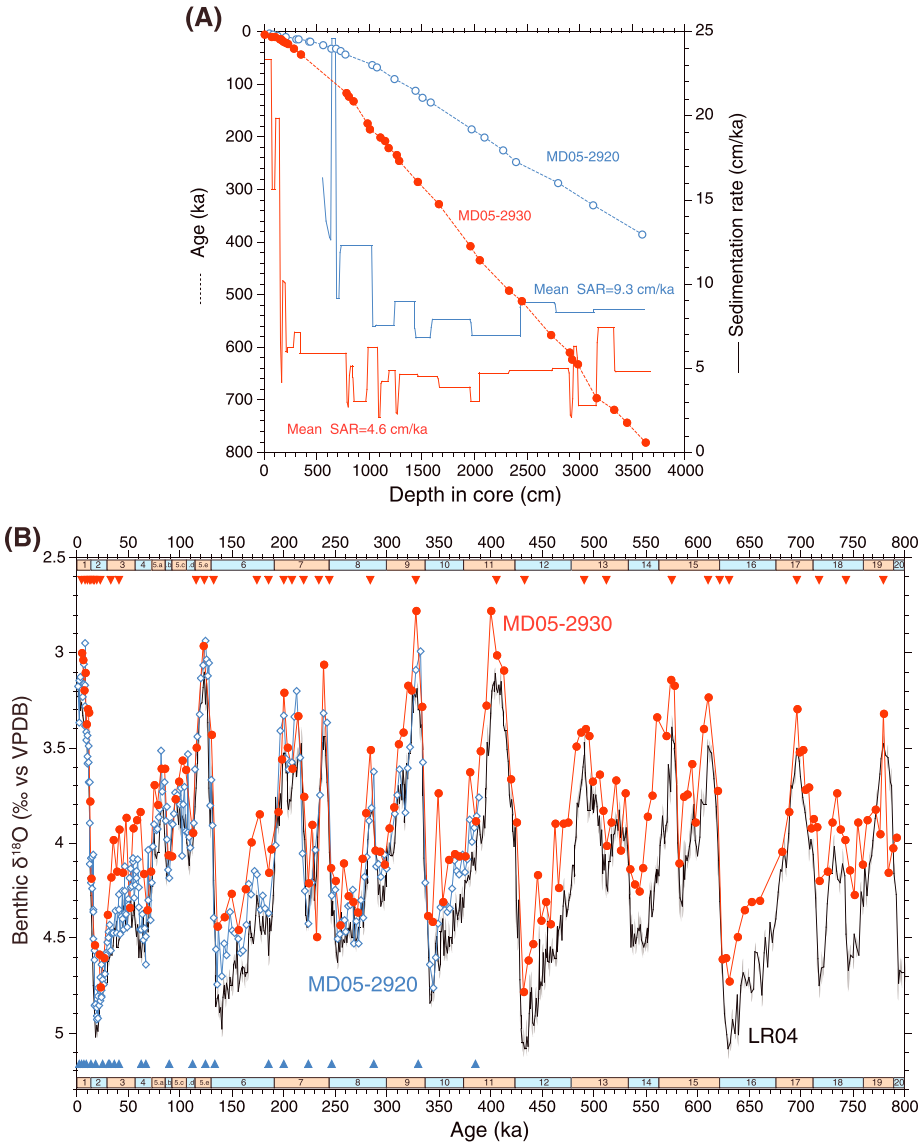

Figure 2. Chronostratigraphy. Oxygen isotope stratigraphy for cores MD05-2920 (blue) and MD05-2930 (red) derived from the $\delta^{18}O$ recorded by benthic foraminifera *Cibicidoides wuellerstorfi* and *Uvigerina peregrina*. Marine oxygen isotope stages are labeled according to the LR04 ages [*Lisiecki and Raymo*, 2005]. (a) Depth-age relationship and derived sedimentation rates of cores MD05-2920 (blue) and MD05-2930 (red). (b) $\delta^{18}O$ records along the reference benthic stack LR04 of *Lisiecki and Raymo* [2005]. The records are placed on their own chronologies. The full-colored triangles locate the radiocarbon ages and correlation tie-points of both cores with the reference record LR04 (see Tables S1 and S2).

20 (5 to 790 ka). The MD90-0961 $\delta^{18}O$ record has been compared with oxygen isotopic stratigraphy from twin core MD90-0963 [*Bassinot et al.*, 1994] in order to derive a chronology that lasts from MIS 9 to MIS 22. The cosmogenic isotope record of core MD90-0961 covers a stratigraphic interval spanning MIS 17 to MIS 22 [*Valet et al.*, 2014]. According to their respective age models, the mean sedimentation rates in cores MD05-2920, MD05-2930, and MD90-0961 are 9.3, 4.6, and 4.7 cm/ka, respectively (Figure 2a).

2.3. Authigenic Beryllium Normalization Procedures

The exchangeable-^{10}Be concentrations measured in the sediments, or authigenic ^{10}Be (i.e., the fraction dissolved or chemically precipitated and adsorbed onto settling particles), do not only reflect atmospheric production at the time of their deposition but also depend on oceanic transport processes and detrital inputs from surrounding continents [*Bourlès et al.*, 1989; *Christl et al.*, 2010; *Simon et al.*, 2016]. The normalization of

authigenic ^{10}Be concentration is necessary to correct for such sedimentary imprints and compare ^{10}Be records with geomagnetic variability. The normalization of the authigenic ^{10}Be cosmogenic nuclide by the authigenic stable ^{9}Be isotope released by silicate rock weathering relies on the similar behavior of both isotopes once homogenized in seawater [*Bourlès et al.*, 1989; *Brown et al.*, 1992]. This method reliably corrects for ocean/continent secondary contributions and provides robust results clearly demonstrating an inverse relationship with the geomagnetic field [e.g., *Henken-Mellies et al.*, 1990; *Robinson et al.*, 1995; *Carcaillet et al.*, 2003, 2004a, 2004b; *Thouveny et al.*, 2008; *Knudsen et al.*, 2008; *Ménabréaz et al.*, 2012, 2014; *Valet et al.*, 2014; *Horiuchi et al.*, 2016].

2.4. Authigenic ^{9}Be and ^{10}Be Extraction and Measurements

Samples of ~1 g (dry sediment) were collected from cores MD05-2920 and MD05-2930 with a 10 cm resolution representing a total of 300 and 378 samples and ~1 to ~2 ka nominal time resolution, respectively. These samples have been processed for the Be isotope analysis at the Centre Européen de Recherche et d'Enseignement de Géosciences de l'Environnement (CEREGE) National Cosmogenic Nuclides Laboratory (France) according to the chemical procedure established by *Bourlès et al.* [1989] and used by subsequent studies from the same group [e.g., *Carcaillet et al.*, 2004b; *Ménabréaz et al.*, 2012, 2014; *Valet et al.*, 2014]. Authigenic ^{10}Be and its stable isotope ^{9}Be were extracted from each ~1 g dry samples by soaking them in 20 mL of 0.04 M hydroxylamine (NH_2OH-HCl) in a 25% acetic acid leaching solution at 95 ± 5°C for 7 h. A 2 mL aliquot of the resulting leaching solution was sampled for the measurement of the natural ^{9}Be concentration. The remaining solution was spiked with 300 µL of a 9.8039×10^{-4} g.g^{-1} ^{9}Be carrier before Be purification by chromatography in order to accurately determine ^{10}Be sample concentrations from the accelerator mass spectrometry (AMS) measurements of ^{10}Be/^{9}Be ratios (additional details on sample preparation and chemical procedures are given in *Simon et al.* [2016]). In addition to sample processing, several routine blanks and replicates were measured in order to evaluate the cleanliness and reproducibility during the chemical extraction.

The natural authigenic ^{9}Be concentrations were measured by using a graphite-furnace atomic absorption spectrophotometer (AAS) with a double-beam correction (Thermo Scientific ICE 3400®). The standard-addition method and the addition of a constant volume of $Mg(NO_3)_2$ solution were used to eliminate the matrix effects during the absorption and to allow measurements near the detection limit. Authigenic ^{9}Be sample concentrations vary around $2.00 \pm 0.38 \times 10^{-7}$ g.g^{-1} (MD05-2920) and $3.03 \pm 0.43 \times 10^{-7}$ g.g^{-1} (MD05-2930). The associated uncertainties (2σ) based on the reproducibility of quadruplicated measurements and the least squares fitting between measured absorbance at each stages of the standard-addition method varying around average values of 1.6% (MD05-2920) and 1.9% (MD05-2930). Similar ^{9}Be concentration range and uncertainty have been measured in core MD90-0961 from the Indian Ocean, i.e., $2.00 \pm 0.32 \times 10^{-7}$ g.g^{-1} and a mean uncertainty of 2.2% [*Valet et al.*, 2014]. The natural authigenic ^{10}Be concentration measurements were performed at the French AMS national facility Accélérateur pour les Sciences de la Terre, Environnement, Risques (ASTER) (CEREGE) [*Arnold et al.*, 2010]. ^{10}Be sample concentrations are calculated from the measured spiked ^{10}Be/^{9}Be ratios normalized to the National Institute of Standards and Technology 4325 Standard Reference Material ($2.79 \pm 0.03 \times 10^{-11}$) [*Nishiizumi et al.*, 2007] and are decay-corrected by using the ^{10}Be half-life ($T_{1/2}$) of 1.387 ± 0.012 Ma [*Chmeleff et al.*, 2010; *Korschinek et al.*, 2010]. The calculations of the radioactive decay of ^{10}Be-concentration results presented in *Ménabréaz et al.* [2014] and *Valet et al.* [2014] have been revised in this study. This is particularly important since we are dealing with multiple records and want to compare ^{10}Be/^{9}Be ratio variation amplitudes through time. Chemistry blank ratios range from 10^{-14} to 10^{-15}, i.e., at least 3 orders of magnitude lower than the sample ^{10}Be/^{9}Be ratios. The authigenic ^{10}Be/^{9}Be ratios are calculated from ^{9}Be-AAS and ^{10}Be-AMS concentration measurements transformed in atoms [*Simon et al.*, 2016]. Associated uncertainties (2σ) are derived from the propagation of both uncertainties and vary around 4.3%, 4.7%, and 5.6% in cores MD05-2920, MD05-2930, and MD90-0961, respectively (see Tables S3–S5).

3. Results

All sample concentrations in atoms per gram and ratios are presented versus depth in Figures 3 and 4. The results and statistical averages are reported hereafter with a $\pm 2\ \sigma$ uncertainty.

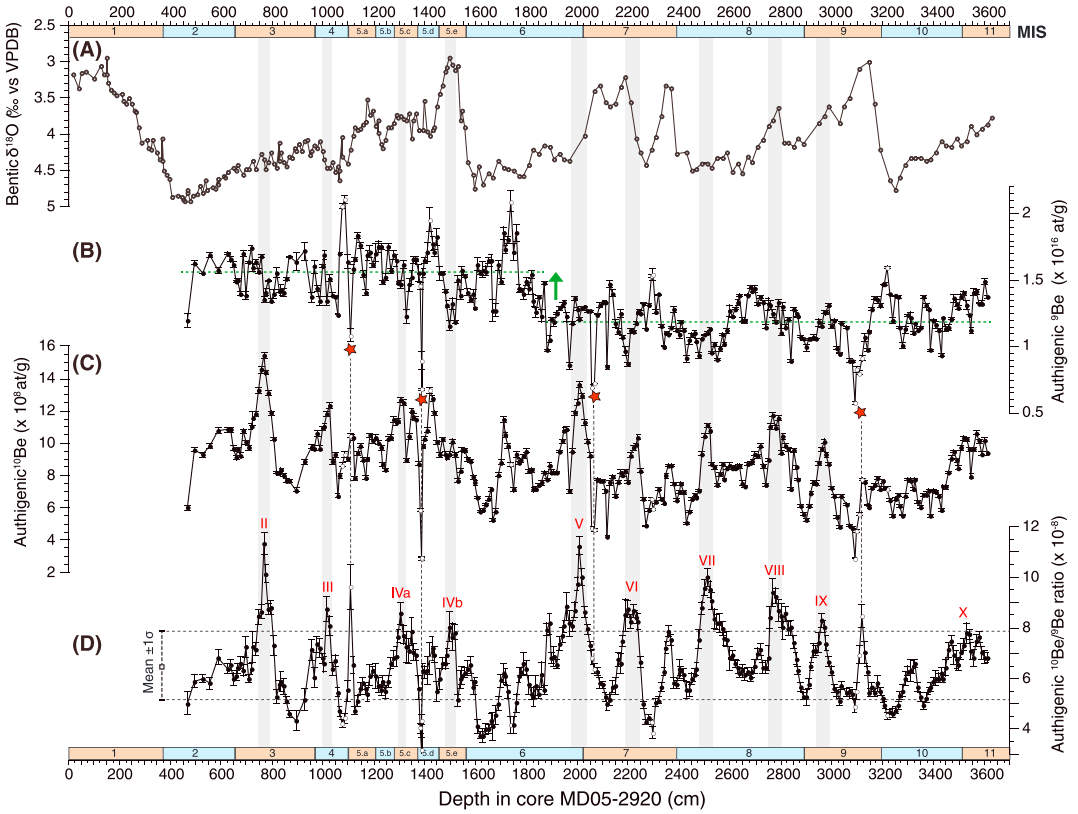

Figure 3. Benthic $\delta^{18}O$ record and authigenic beryllium isotope results from core MD05-2920. (a) The oxygen isotope record from benthic foraminifera *Cibicidoides wuellerstorfi* and *Uvigerina peregrina* is expressed as $\delta^{18}O$ versus VPDB (‰). (b) Authigenic ^{9}Be concentration variations present a significant change at 1820 cm. The green dotted lines represent mean values computed over each interval (467 to 1820 cm and 1820 to 3610 cm). The white dots represent sample outliers from both intervals (data outside mean $\pm 1.96\sigma$, $p = 0.05$) associated to sharp paleoenvironmental events (these levels are also represented by the white dots in Figures 3c and 3d). The red stars identify tephra layers recognized by magnetic susceptibility spikes. (c) The decay-corrected authigenic ^{10}Be concentrations reveal successive intervals of significant increase and three sharp minima. Three large ^{10}Be lows correspond to ^{9}Be minima associated with the tephra layers (dashed line). (d) Authigenic $^{10}Be/^{9}Be$ ratio with mean $\pm 1\sigma$. The $^{10}Be/^{9}Be$ ratio increase intervals are highlighted by the vertical gray bars and numbered from II to X according to the labeling system proposed by *Carcaillet et al.* [2004a] and *Ménabréaz et al.* [2014].

3.1. Authigenic ^{9}Be Concentration

The authigenic ^{9}Be concentrations vary from 0.58 to 2.11×10^{16} at.g^{-1} in core MD05-2920 with an average value and standard deviation of $1.34 \pm 0.25 \times 10^{16}$ at.g^{-1} (Figure 3b). Higher values ranging from 1.14 to 3.00×10^{16} at.g^{-1} with an average value and standard deviation of $2.03 \pm 0.29 \times 10^{16}$ at.g^{-1} are observed throughout core MD05-2930 (Figure 4b). The highest ^{9}Be concentration range is found within the core presenting the lowest sedimentation rates (MD05-2930), contrary to what had been observed on Portuguese margin sediments [*Carcaillet et al.*, 2004b]. This is likely explained by different Be scavenging affinity with particle type: i.e., higher carbonate content in core MD05-2920 compared to siliciclastic sediments of core MD05-2930 [*Chase et al.*, 2002]. This interpretation is supported by similar ^{9}Be concentration ranges measured in carbonate-rich MD90-0961 [*Valet et al.*, 2014] and MD05-2920 cores. Four ^{9}Be-concentration lows (Figure 3b) in core MD05-2920 coincide with layers enriched in tephra material characterized by high magnetic susceptibilities. Extreme ^{9}Be-concentration values in both cores, outside from the 95% normal distribution, are represented by the white dots in Figures 3b and 4b. The long-term average ^{9}Be concentration of core MD05-2920 presents a major change at mid-MIS 6 stage (near 165 ka). Average values vary significantly around (i) 1.19 ± 0.17 at.g^{-1} beneath 1829 cm and (ii) 1.56 ± 0.18 at.g^{-1} between 1820 and 0 cm (Figure 3b). Such a significant shift is not observed neither in the $\delta^{18}O$ signals nor in the XRF data [*Tachikawa et al.*, 2011, 2014], precluding a simple climatic interpretation. A slight increasing trend of Fe percentage accompanied

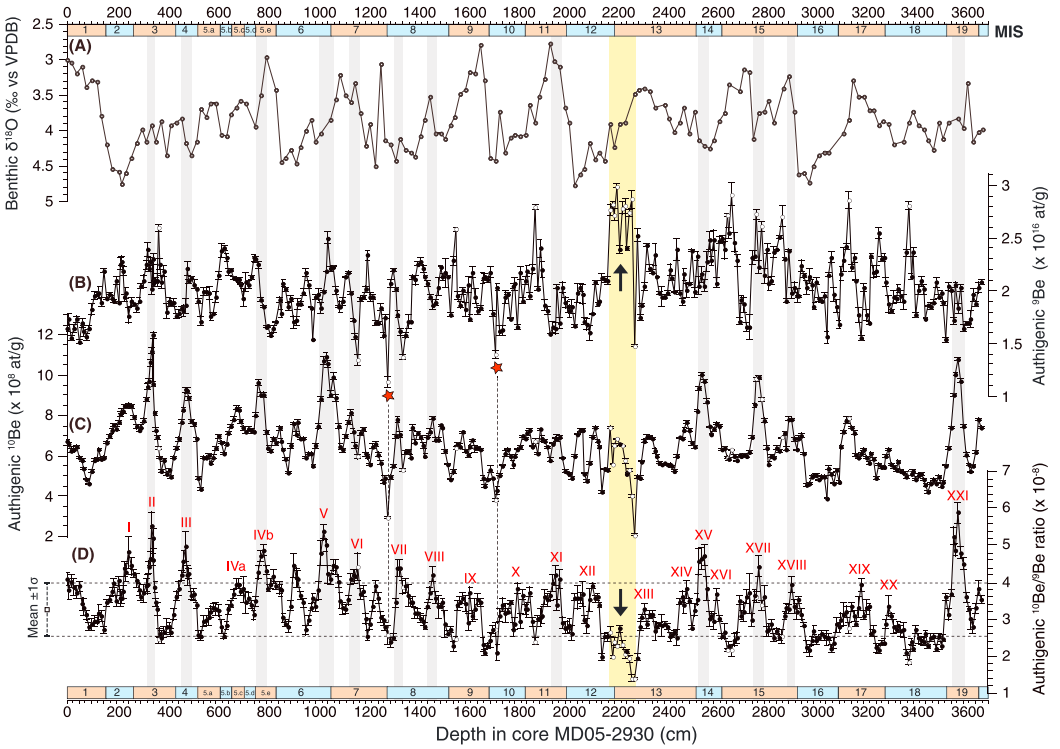

Figure 4. Benthic $\delta^{18}O$ record and authigenic beryllium isotope results from core MD05-2930. (a) The oxygen isotope record from benthic foraminifera *Cibicidoides wuellerstorfi* and *Uvigerina peregrina* is expressed as $\delta^{18}O$ versus VPDB (‰). (b) Authigenic ^{9}Be concentration variations present increase intervals corresponding to transition from interglacial to glacial periods. The white dots represent sample outliers (data outside mean $\pm$ 1.96σ, $p = 0.05$) associated to sharp paleoenvironmental events (these levels are also represented by the white dots in Figures 3c and 3d. The red stars identify tephra layers recognized by magnetic susceptibility spikes. Large ^{9}Be concentrations highlighted by vertical yellow bar are found at 2180–2280 cm depth corresponding to the transition between MIS 12 and 13 periods. (c) The decay-corrected authigenic ^{10}Be concentrations reveal successive intervals of significant increase and two sharp minima. The ^{10}Be-peaks are not related to major ^{9}Be changes, while minimum ^{10}Be-concentrations are found at depth embedded within sharp environmental imprint (white dots). (d) Authigenic $^{10}Be/^{9}Be$ ratio with mean $\pm$ 1σ.

with a decreasing trend of the $CaCO_3$% suggests a progressive intensification of the rivers discharges, and dissolved ^{9}Be delivery into the Bismarck Sea, highlighting the role of past hydrological changes on the sediment composition of core MD05-2920 [*Tachikawa et al.*, 2011]. Five ^{9}Be-concentration peaks, statistically distinct from the long-term average of each interval, are observed during glacial periods (MIS 4, 5.d, 6, 7.d, and 10) likely supporting sharp paleoenvironmental changes at these levels. In contrast with core MD05-2920, the authigenic ^{9}Be concentrations of core MD05-2930 do not show any clear trend but exhibit some sharp ^{9}Be-concentration increases at transition intervals between interglacial and glacial periods (Figure 4b). This timing corresponds to periods characterized by sea level drops, oceanic circulation, and water-column property (e.g., thermocline depth) changes that contribute to modify drastically the sedimentation realm within the GOP [*Jorry et al.*, 2008]. While ^{9}Be-concentration peaks are generally rather small, a large interval of high ^{9}Be concentrations is found between 2180 and 2280 cm, at the transition between MIS 12 and 13. Strong correlation with terrigenous proxies such as Ti or Fe elemental concentrations supports a close association of ^{9}Be signature with terrigenous signals (Tachikawa, personal communication) highlighting the influence of sea level changes on ^{9}Be input in the GOP. During sea level lowstands (glacials), the large and shallow continental margin between Australia and Papua New Guinea was subaerially exposed, the main rivers extended to the present shelf edge and reef systems karstified. This led to an increased dilution of the carbonate fluxes by the siliciclastic fluxes explaining the relatively high ^{9}Be concentration of these layers.

3.2. Authigenic ^{10}Be Concentration

Authigenic ^{10}Be (decay-corrected) concentrations vary from 2.84 to 15.39 $\times 10^{8}$ at.g^{-1} in core MD05-2920 with an average value of 8.6 $\pm$ 2.0 $\times 10^{8}$ at.g^{-1}. Smaller variations are observed in core MD05-2930 with

authigenic ^{10}Be (decay-corrected) concentrations ranging from 2.08 to 12.00×10^8 at.g^{-1} and an average value of $6.6 \pm 1.4 \times 10^8$ at.g^{-1}. The main ^{10}Be-concentration features of both cores are the presence of large peaks and some sharp minima (Figures 3c and 4c). The ^{10}Be intervals that correspond to extreme ^{9}Be-concentration values, outside from the 95% normal distribution, are represented by the white dots in Figures 3c and 4c. In core MD05-2920, the decay-corrected authigenic ^{10}Be-concentrations denote several important increase intervals and three sharp minima. These ^{10}Be lows correspond to major ^{9}Be changes associated with tephra layers at 1387, 2059–2069, and 3089–3119 cm. The ^{10}Be concentrations yield a slightly increasing trend through the MD05-2920 core ($r^2 = 0.2$) similar to its ^{9}Be concentration variation (Figure 3b). This observation is coherent with regional hydrological cycle variations and the progressive intensification of rivers discharge that likely support higher scavenging rates of dissolve Be isotopes from the water column. Core MD05-2930 does not display any trend in the ^{10}Be-concentration signature but exhibits seven large peaks and three lows. Two of these low ^{10}Be-concentration intervals, i.e., 1290 and 1720 cm, correspond to major ^{9}Be lows associated with magnetic susceptibility spikes related to tephra layers. The interval at 2280 cm that presents the lowest ^{10}Be-concentration value is also characterized by a significant ^{9}Be-concentration low associated with a major environmental change immediately prior to the 2180–2280 cm interval (highlighted by a yellow bar in Figure 4). Detailed comparison of authigenic Be concentration signals with environmental proxies along the MD05-2920 and MD05-2930 cores is beyond the scope of this paper; however, for few specific layers the homogeneous mixing of both dissolved ^{10}Be and ^{9}Be isotopes in the water column has been questioned, stressing the need for cautious geomagnetic interpretations of the authigenic ^{10}Be/^{9}Be ratios in these intervals.

3.3. Authigenic ^{10}Be/^{9}Be Ratio

The authigenic ^{10}Be/^{9}Be ratio varies from 3.68 to 11.35×10^{-8} and 1.40 to 5.90×10^{-8} in cores MD05-2920 and MD05-2930, respectively. The long-term average value of core MD05-2920 is $6.50 \pm 1.34 \times 10^{-8}$, 2 times higher than the long-term mean value from core MD05-2930, $3.26 \pm 0.72 \times 10^{-8}$. This difference is mainly supported by higher ^{9}Be-concentration variations (about 75% of the variance) and, to a lower degree, by ^{10}Be-concentration changes. The authigenic ^{10}Be/^{9}Be ratio from core MD90-0961 varies from 2.26 to 8.27×10^{-8} and presents a long-term average of $3.93 \pm 1.35 \times 10^{-8}$ [*Valet et al.*, 2014]. Interestingly, the ~2:1 ratio between the mean ^{10}Be/^{9}Be ratios is similar to the sedimentation rate ratios between those cores supporting a direct link between siliciclastic sedimentation rates and scavenging efficiency. Three of the four intervals from core MD05-2920 that present large ^{9}Be-concentration lows associated with tephra layers (red star in Figure 3b) yield significantly distinct ^{10}Be/^{9}Be ratios (Figure 3d). In core MD05-2930, the interval 2180–2280 cm associated with large ^{9}Be- and ^{10}Be-concentration variations clearly shows a substantial ^{10}Be/^{9}Be ratios inconsistency (Figure 4d). These intervals associated with environmental artefacts represent less than 3% of the total samples from both cores (5 samples over 300 and 10 samples over 378 in cores MD05-2920 and MD05-2930, respectively). Other samples presenting large ^{9}Be concentration changes likely associated with environmental imprints (white dots in Figures 3d and 4d) yield coherent ^{10}Be/^{9}Be ratio with their neighbor samples. Furthermore, no similarities nor correlations are observed between the authigenic ^{10}Be/^{9}Be ratio series and δ^{18}O records or their ^{9}Be normalizer ($r^2 < 0.1$), supporting the ^{9}Be normalization method, even within the intervals characterized by rapid environmental changes.

Despite some amplitude differences, the two authigenic ^{10}Be/^{9}Be ratio records exhibit similar series of peaks (Figures 3d and 4d). Intervals characterized by ^{10}Be/^{9}Be ratio increases are numbered from I to XXII according to the labeling system proposed by *Carcaillet et al.* [2004a] and used by *Ménabréaz et al.* [2014]. Eventually, these labels are accompanied by the names of documented geomagnetic excursions for comparison purpose (Table 1). When compared to the long-term average Be ratio values, all peaks labeled along the MD05-2920 and MD05-2930 represent a multiplication by 1.2 to 1.8. When compared with the framing Be ratio, they represent multiplication factors up to 2.1 (Figures 3d and 4d). In the two cores MD05-2920 and MD05-2930, the averages of the highest ^{10}Be/^{9}Be values (above the mean + 1σ) are 8.7×10^{-8} and 4.5×10^{-8}, respectively, and are about 2 times higher than the averages of the lowest values (below mean-1σ), 4. 6×10^{-8} and 2.4×10^{-8}, respectively. In core MD90-0961 where the measured series covers mainly the interval containing the polarity transition, this ratio is 2.7.

Journal of Geophysical Research: Solid Earth

10.1002/2016JB013335

Table 1. Authigenic ^{10}Be/^{9}Be Increase Periods in the MD05-2920, MD05-2930, and MD90-0961 Stack Compare to Corresponding Geomagnetic Dipole Lows (GDL) From References

Stack ^{10}Be/^{9}Be Ratio Peaks						Category[e] 2 of ^{10}Be Overproduction, Deviation > 1σ				Category 1 of ^{10}Be Overproduction, Deviation > 2σ						
Labels[a]	Age (ka)	Enhancement Factor[b]	Standardized Values[c]	^{10}Be-Derived VADM (10^{22} Am^2)	% of the Average Field[d]	Time Interval (ka)	Duration (ka)	^{10}Be-Derived VADM (10^{22} Am^2)	% of the Average Field	Time Interval (ka)	Duration (ka)	^{10}Be-Derived VADM (10^{22} Am^2)	% of the Average Field	GDL Label[f]	Names potentially associated to excursions[g]	Marine Oxygen Isotope Stages
I*	27	1.23	1.09	3.81	51.57	27–28	1	3.84	51.9						Rockall/Mono Lake (3α)	2/3
II*	41	1.60	2.89	1.34	18.09	39–44	5	2.63	35.6	40–42	2	1.36	18.4	a	Laschamp (3β)	3
III*	62	1.28	1.33	3.33	45.07	61–65	4	3.69	49.8					a′	Norwegian Greenland Sea (4α)	4
IVa*	98	1.22	1.05	3.91	52.91	98	<1	3.91	52.91					b1	Post-Blake/ Fram Strait I (5α)	5.3
IVb*	119	1.24	1.12	3.74	50.57	118–120	2	3.84	52.0					b2	Blake (5β)	5.5
V*	190	1.66	3.16	1.21	16.36	187–194	7	2.44	33.0	188–191	3	1.60	21.6	c	Iceland-Basin (7α)	6/7
VI*	217	1.32	1.53	2.96	40.04	212–219	7	3.30	44.7					d	Pringle-Falls ((7β)	7
VII	258	1.43	2.06	2.14	28.91	256–263	7	3.06	41.4	258	<1	2.14	28.9		Calabrian Ridge 0/Fram Strait (8α)	8
VIII	286	1.33	1.57	2.90	39.18	284–288	4	3.39	45.8					g	Portuguese margin	8
IX	309	1.14	0.70	4.77	64.47		n.s.[h]							h	Calabrian Ridge 1 (9α)	9
X	378	1.11	0.52	5.22	70.53	n.s.								i1	Laguna del Sello/Levantine/ Bermuda (11β)	10/11
XI	406 (412)	1.26 (1.21)	1.23 (1.01)	3.51 (3.99)	47.5 (53.9)	404–406 (412)	2 (+1)	3.73	50.4					i2		11
XII	(438) 447	1.11 (1.17)	(0.52) 0.82	5.20 (4.41)	70.2 (59.6)	n.s.								j1 & j2	Emperor	12
XIII	491	0.98	−0.07	6.95	93.92	n.s.								k	(13α)	13
XIV	523	1.13	0.64	4.88	66.02	n.s.								l1	Big Lost/	13
XV	538	1.43	2.02	2.15	29.02	534–540	6	2.50	33.8	538	<1	2.15	29.0	l2	Calabrian	13/14
XVI	550	1.09	0.43	5.43	73.37	n.s.								m	Ridge 2/West Eifel 4 and 5/ (14α)	14
XVII	586	1.34	1.61	2.78	37.58	585–586	1	3.38	45.7					n	Calabrian Ridge 3 / Los Tilos / La Palma (15β)	15
XVIII	615	1.2	0.93	4.16	56.28	n.s.								o	La Palma (15β)/ West Eifel 2	15/16
XIX	700	1.1	0.44	5.26	71.15	n.s.								p, q	Stage 17 (17α)/ Delta	17
XX	715	0.81	−0.55	10.00	135.26			n.s.						r	West Eifel 1	18

Table 1. (continued)

		Stack $^{10}Be/^{9}Be$ Ratio Peaks				Category[e] 2 of ^{10}Be Overproduction, Deviation $> 1\sigma$				Category 1 of ^{10}Be Overproduction, Deviation $> 2\sigma$					
Labels[a]	Age (ka)	Enhancement Factor[b]	Standardized Values[c]	^{10}Be-Derived VADM (10^{22} Am^2)	% of the Average Field[d]	Time Interval (ka)	Duration (ka)	^{10}Be-Derived VADM (10^{22} Am^2)	% of the Average Field	Time Interval (ka)	Duration (ka)	^{10}Be-Derived VADM (10^{22} Am^2)	% of the Average Field	GDL Label[f]	Names potentially associated to excursions[g]	Marine Oxygen Isotope Stages
XXI	772	1.84	3.16	1.24	16.77	765–777	12	1.46	19.8	767–775	8	1.23	16.7	s	Brunhes/ Matuyama transition (B/M)	19
XXII*	839	1.36	1.05	2.61	35.33	839–840	1	2.64	35.7						Kamikatsura	21

[a] Adapted following the nomenclature proposed by *Ménabréaz et al.* [2014]. Stared roman numbers (*) are from this study.
[b] The long-term average of the normalized stack.
[c] The distance to the mean, expressed in units of the standard deviation, of the arithmetic stack constructed from each standardized records ($(x_i\text{-mean})/\sigma$) and sampled at 1 ka interval.
[d] The long-term average geomagnetic dipole moment covering the 5–850 ka period derived from the authigenic $^{10}Be/^{9}Be$ ratios stack = $7.4 \pm 2.7 \times 10^{22}$ Am^2.
[e] The clustering is based on standard deviation values from the standardized stack.
[f] According to a nomenclature proposed by *Thouveny et al.* [2008] and used in *Ménabréaz et al.* [2014].
[g] Names are used here for clarity only and are those cited in *Langereis et al.* [1997], *Channell et al.* [2006, 2016], *Lund et al.* [2001, 2006], *Laj and Channell* [2015]; *Singer et al.* [2002, 2005, 2008a, 2008b, 2014], and *Thouveny et al.* [2004, 2008].
[h] n.s. indicates nonsignificant (<1 standard deviation) $^{10}Be/^{9}Be$ ratio enhancement.

4. Authigenic $^{10}Be/^{9}Be$ Ratio Stack

All authigenic $^{10}Be/^{9}Be$ ratio records are presented on their respective time scales and discussed in the chronological context (Figures 5–7). Figure 5a presents the standardized $^{10}Be/^{9}Be$ ratio records of the MD05-2920, MD05-2930, and MD90-0961 cores. The three records exhibit authigenic $^{10}Be/^{9}Be$ ratio enhancements interpreted as the results of geomagnetic dipole lows (GDLs) which occurred over the covered time span: the last 850 ka. This interpretation can be assessed by comparison with the RPI stacks SINT-2000 [*Valet et al.*, 2005] and PISO-1500 [*Channell et al.*, 2009] (Figures 5d and 5e). In these RPI reference curves GDL intervals have been labeled from a to u (Figures 5 and 6), following *Thouveny et al.* [2008]. The overall agreement between the overlapping parts of the three records and the correspondence of $^{10}Be/^{9}Be$ ratio peaks with GDLs confirms that the main signal responds to the ^{10}Be overproduction under global geomagnetic modulation (Figures 5 and 6d). An averaged ^{10}Be production record was constructed by stacking the three authigenic $^{10}Be/^{9}Be$ ratio records by using two distinct methods presented in Figures 5b–5d. The first method uses series normalized to their own long-term mean (Figure 5b). The second method uses records standardized to their own mean and standard deviation value (Figure 5c). Both methods yield similar results. Each normalized and standardized records have been linearly re-sampled at 1 ka interval, corresponding roughly to the average sampling resolution of core MD05-2920, prior to stacking. The averaging was performed by computing arithmetical means along each individual $^{10}Be/^{9}Be$ ratio record. The uncertainties were calculated by error propagation where cores overlapped and correspond to analytical uncertainty of the MD05-2930 core within the 387–685 ka interval (Figure 5). These errors likely represent minimal uncertainty. Further, $^{10}Be/^{9}Be$ ratio and $\delta^{18}O$ results from additional records will contribute to increase the global and temporal resolutions of our regional stack, strengthening its interpretation.

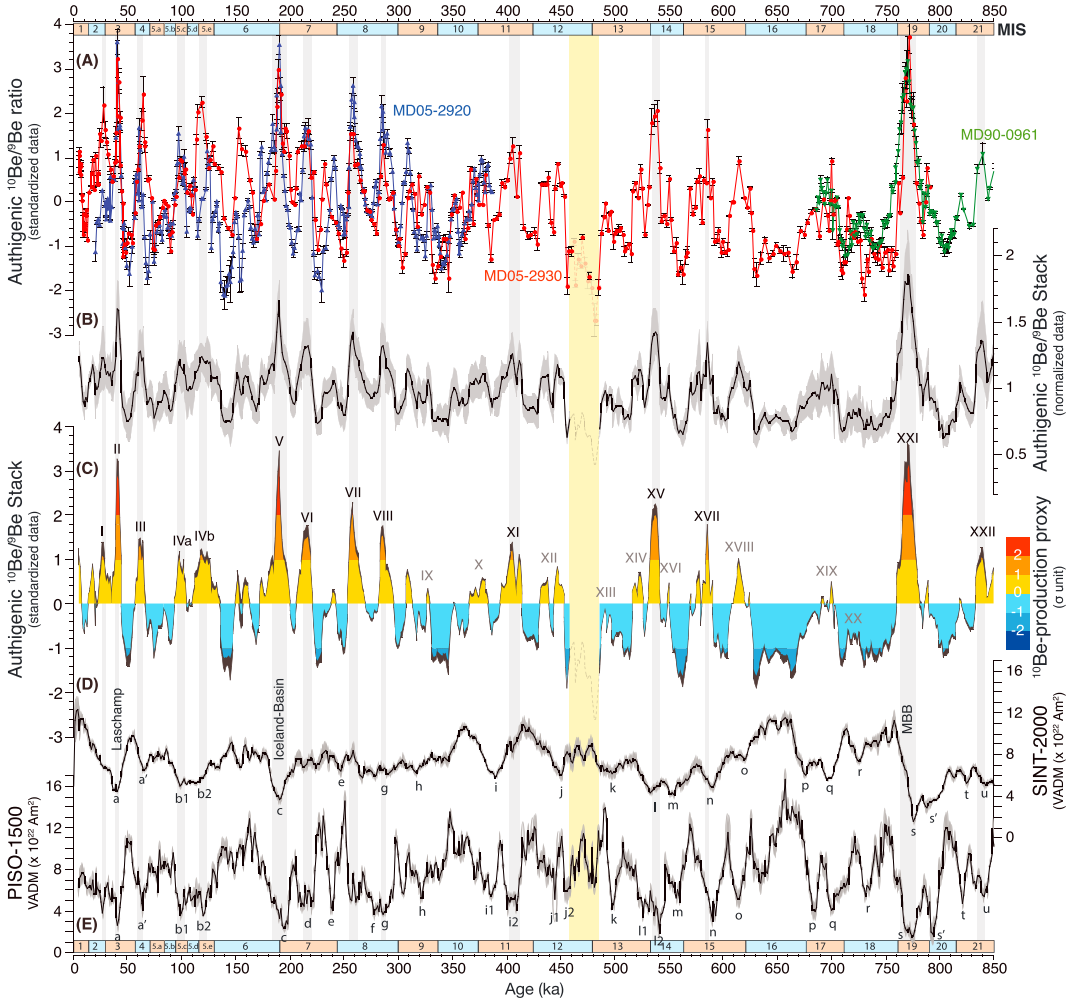

Figure 5. Authigenic ^{10}Be/^{9}Be ratio records and stacks from cores MD05-2920, MD05-2930, and MD90-0961 compared with two published VADM stacks. All records are plotted on their respective time scales. (a) Standardized authigenic ^{10}Be/^{9}Be ratios for cores MD05-2920 (blue), MD05-2930 (red), and MD90-0961 (green). (b) Normalized and (c) Standardized ^{10}Be/^{9}Be ratio partial stacks computed from the three core records. VADM variations reconstructed from the (d) SINT-2000 [*Valet et al.*, 2005] and the (e) PISO-1500 [*Channell et al.*, 2009] RPI stacks. The ^{10}Be/^{9}Be ratio increase intervals are highlighted by the vertical gray bars and labeled by roman numerals. Atmospheric ^{10}Be-production increases are synchronous with geomagnetic dipole lows (GDLs) that are labeled by letters from a to u (according to *Thouveny et al.* [2008]) on the SINT-2000 and PISO-1500 records. The vertical yellow bar highlights the disturb interval exclude for the geomagnetic interpretation.

The standardized stack provides a straightforward means for clustering the ^{10}Be overproduction episodes (Figure 5c). The stack exhibits major ^{10}Be production peaks (defined by ^{10}Be/^{9}Be ratios higher than the long-term average +2σ) at intervals II, V, VII, XV, and XXI. Significant increases are defined by ^{10}Be/^{9}Be ratios higher than the long-term average +1σ. Other minor increases, characterized by ^{10}Be/^{9}Be ratios lower than long-term average +1σ, are related to GDLs in the SINT-2000 and/or PISO-1500 records. A comprehensive interpretation of these three categories of ^{10}Be/^{9}Be ratio increase intervals, and their relationships with reported geomagnetic excursions, is proposed in the following section (Table 1).

5. Interpretation of the Authigenic ^{10}Be/^{9}Be Ratio Variation

This new record is characterized by the compilation of multiple records over the 20–386 ka and the 688–790 ka intervals. The results from the 280–790 ka interval obtained from core MD05-2930 are those from *Ménabréaz et al.* [2014], after an appropriate correction of the radioactive decay and slight modification of the

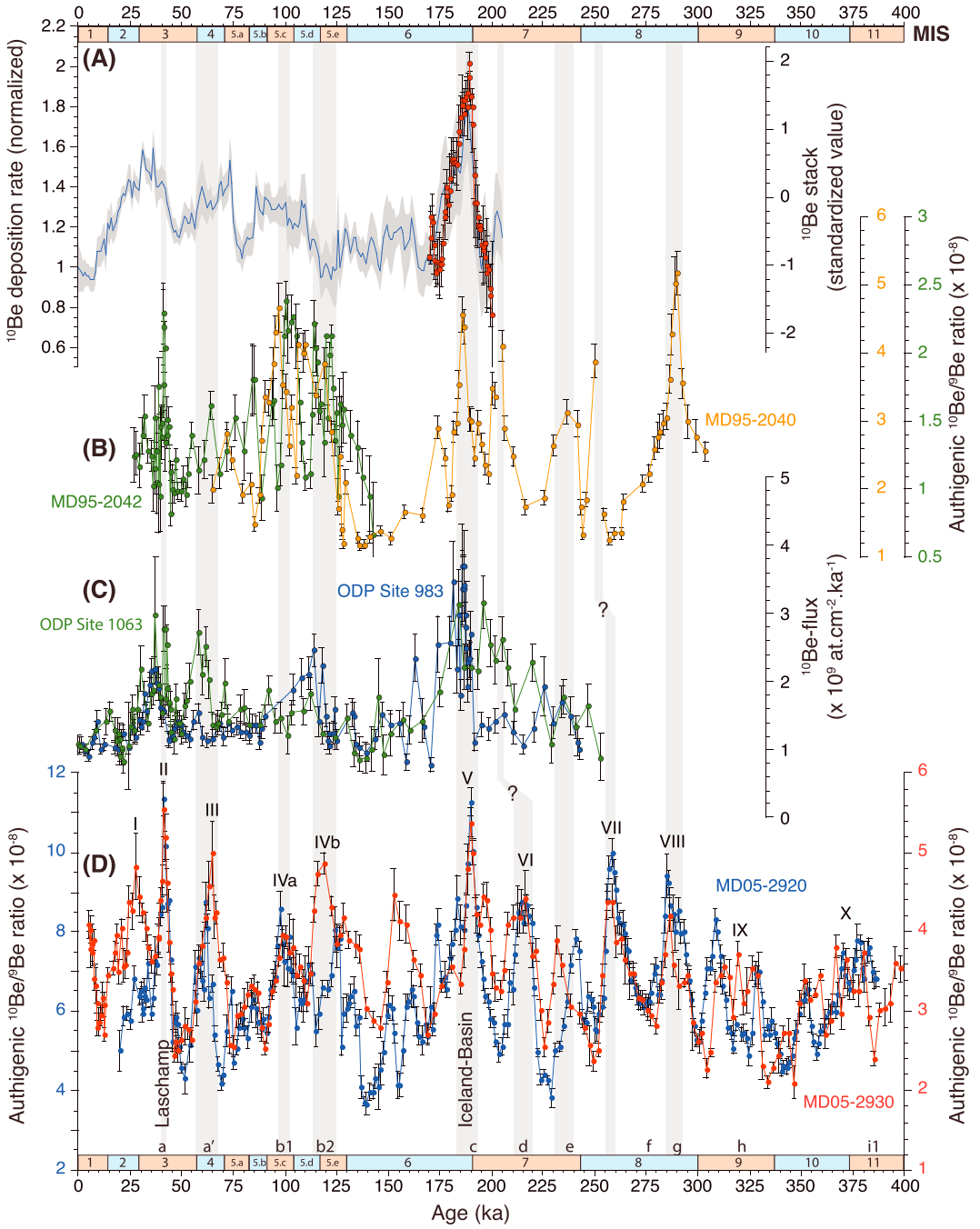

Figure 6. Authigenic ^{10}Be/^{9}Be ratio results over the 0–400 ka interval compared with results of previous studies (see Figure 1 for core locations). (a) Stack of KR0515-PC2 and KR0515-PC4 and Dome Fuji ^{10}Be flux (red dots) across the Iceland Basin excursion (IBE) [*Horiuchi et al.*, 2016]. Normalized ^{10}Be deposition rates (blue line) [*Frank et al.*, 1997]. (b) Authigenic ^{10}Be/^{9}Be ratio records from Portuguese margin cores [*Carcaillet et al.*, 2004a, 2004b]. (c) ^{10}Be flux (^{230}Th$_{xs}$-normalized) from ODP Sites 1063 and 983 [*Knudsen et al.*, 2008; *Christl et al.*, 2010]. (d) Authigenic ^{10}Be/^{9}Be ratio results from core MD05-2920 (blue) and MD05-2930 (red) (this study).

chronology (see section 2.2). The long-term average has been computed over the whole time interval (i.e., the last 850 ka interval that includes the Brunhes Chron and the terminal part of the Matuyama Chron). The ^{10}Be overproduction episodes are described following the three categories defined from the standardized stack (Figure 5c). Category 1 represents standardized values above 2σ. Category 2 includes ^{10}Be overproduction episodes comprise between 1σ and 2σ. Category 3 represents some minor increase intervals below 1σ (see

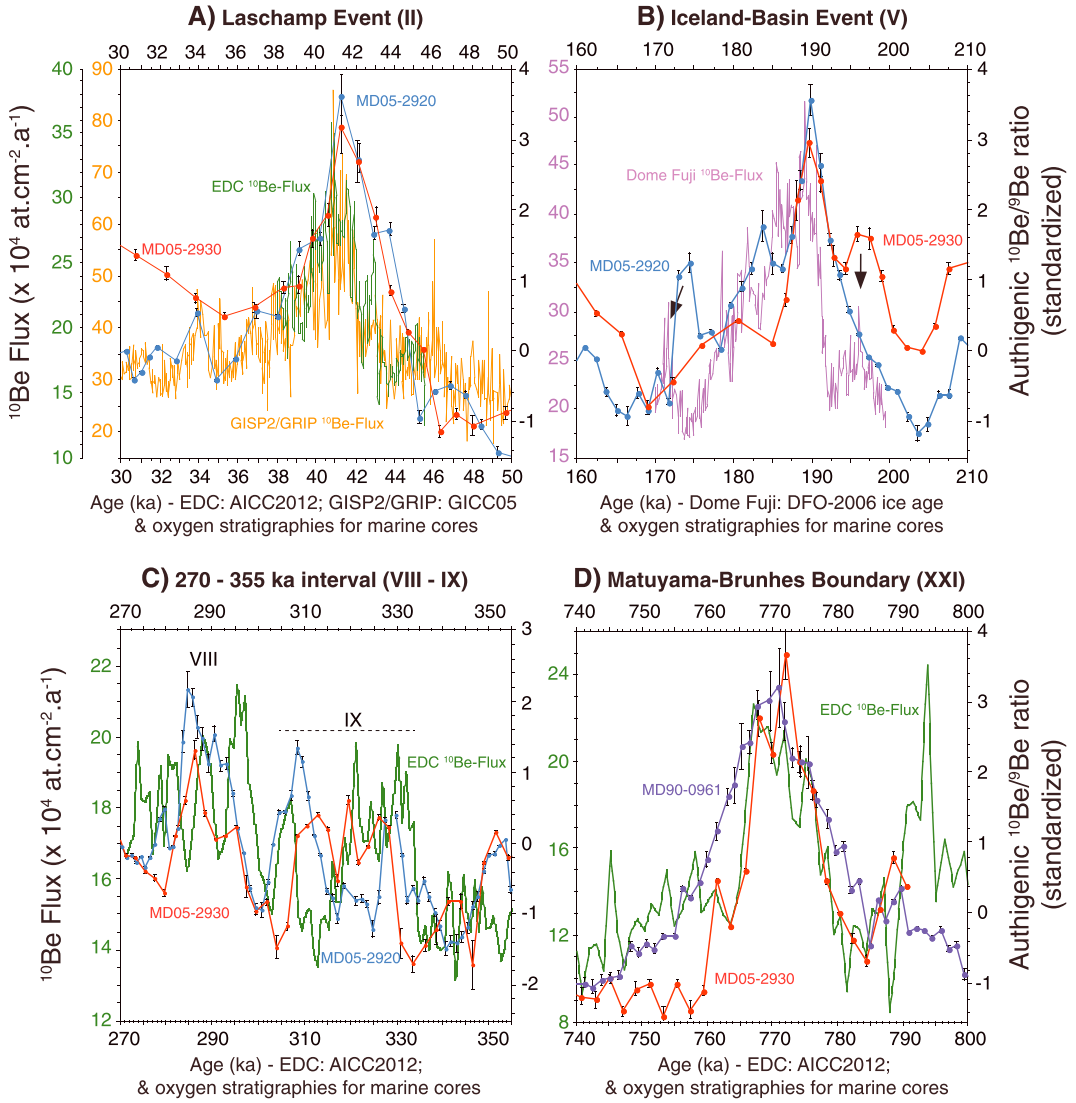

Figure 7. Snapshots of authigenic $^{10}Be/^{9}Be$ ratio results versus ice core records for the (a) Laschamp excursion (LE), (b) Iceland Basin event (IBE), (c) 270–355 ka interval, and (d) the Matuyama-Brunhes Boundary (MBB). We used the standardized records of both MD05-2920, MD05-2930, and MD90-0961 cores plotted on their respective time scales. EDC ^{10}Be fluxes [*Cauquoin et al.*, 2015; *Raisbeck et al.*, 2006, 2007] are plotted on the AICC2012 ice age [*Bazin et al.*, 2013]. GISP2/GRIP ^{10}Be flux [*Muscheler et al.*, 2005] is plotted on the GICC05 time scale [*Svensson et al.*, 2008]. Dome Fuji ^{10}Be-flux [*Horiuchi et al.*, 2016] is plotted on the DFO-2006 ice age time scale [*Kawamura et al.*, 2007].

Table 1 for summary). The sampling resolution together with the stacking process prevents any interpretation with higher resolution than 1 ka.

5.1. Category 1 ^{10}Be Overproduction Episodes

Interval II documents a large $^{10}Be/^{9}Be$ ratio increase representing a ^{10}Be overproduction episode associated with the Laschamp excursion. The 1.8- and 1.7-fold $^{10}Be/^{9}Be$ ratio increase in core MD05-2920 and MD05-2930, respectively, are very similar with the Laschamp GDL in the global paleointensity stack (GLOPIS) [*Laj et al.*, 2004], SINT-2000, and PISO-1500 records (Figure 5). This major $^{10}Be/^{9}Be$ ratio increase (values above 2σ) spans a 2 ka duration interval within the interpolated stack record and appears shorter within individual records (~1 ka). It is globally coherent with ^{10}Be overproduction signal from other marine sequences [*Carcaillet et al.*, 2004b; *Christl et al.*, 2010] (Figures 6b and 6c) and is contemporaneous and similar to a ^{10}Be-flux doubling in ice core records from Antarctica (European Project for Ice Coring in Antarctica

(EPICA) Dome C) [*Raisbeck et al.*, 2007] and Greenland (Greenland Ice Core Project/Greenland Ice Sheet Project 2 (GRIP/GISP2)) [*Muscheler et al.*, 2005] (Figure 7a).

Interval V shows a significant ^{10}Be overproduction episode lasting 3 ka at the MIS 6/7 boundary (Figure 5). The 1.7- and 1.6-fold ^{10}Be/^{9}Be ratio increase in cores MD05-2920 and MD05-2930, respectively, is centered at 190 ka. This corresponds to GDL associated with the Iceland Basin excursion (IBE) [*Channell et al.*, 1997; *Channell*, 1999, 2014; *Laj et al.*, 2006]. The directional swings and RPI low reported for this excursion and GDL yield a midpoint age of 190 ka at eight North Atlantic sites [*Channell*, 1999, 2014], on the Portuguese margin [*Thouveny et al.*, 2004], at the South Atlantic Ocean Drilling Program (ODP) Site 1089 [*Stoner et al.*, 2003], and at western equatorial Pacific Ocean sites [*Yamazaki and Yoka*, 1994]. The IBE GDL also lies in the MIS 6/7 transition in the Lake Baikal records [*Oda et al.*, 2002; *Demory et al.*, 2005]. The IBE corresponds to the GDL c in the SINT-2000 and PISO-1500 records (Figures 5d and 5e). It is synchronous with ^{10}Be overproduction signal reported from several marine records worldwide [*Frank et al.*, 1997; *Carcaillet et al.*, 2004b; *Knudsen et al.*, 2008; *Christl et al.*, 2010; *Horiuchi et al.*, 2016] (Figure 6) and is expressed by a doubling of the ^{10}Be flux recorded in the Antarctica Dome Fuji ice core [*Horiuchi et al.*, 2016] (Figure 7b).

Interval VII shows a large ^{10}Be production enhancement within the 256–263 ka interval. The peak centered at ~258 ka presents a 1.5- and -1.3-fold ^{10}Be/^{9}Be ratio increase in cores MD05-2920 and MD05-2930, respectively. It is not directly related to a major GDL in the RPI stacks (Figures 5d and 5e) but may correspond to few events such as the Calabrian Ridge 0 excursion reported from the Ionian Sea (Mediterranean Sea) by *Langereis et al.* [1997], the 8α excursion described from Integrated Ocean Drilling Program Leg 172 Sites 1060–1063 by *Lund et al.* [2001], and the Fram strait excursion [*Nowaczyk and Frederichs*, 1999].

Interval XV yields a major (1.4-fold increase) ^{10}Be production episode centered at 538 ka associated with GDL l in SINT-2000 and l2 in PISO-1500. It is the major event of a multiple structure composed of three distinct ^{10}Be overproduction peaks: XIV (522–529 ka), XV (534–540 ka), and XVI (550 ka), respectively, related to GDL l and m in SINT-2000, and to GDL l1, l2, and m in PISO-1500. These peak intervals can be tentatively correlated with several identified excursions (Table 1). Interval XV is at the age of prominent RPI lows and excursional directions at Sites 983 and 984 [*Channell et al.*, 2004] and at ODP Site 1062 (14α) [*Lund et al.*, 2001]. The so-called Big Lost excursion was first described in lava flows from Idaho dated at 565 ± 14 ka [*Champion et al.*, 1988] and re-dated at 558 ± 20 ka [*Lanphere*, 2000]; anomalous directions and weak paleointensities in lava flows of the Eifel dated by ^{40}Ar/^{39}Ar at 555 ± 4 ka supported its global occurrence [*Singer et al.*, 2008a].

Interval XXI displays the largest authigenic ^{10}Be/^{9}Be ratio peak (1.8-fold increase compared to the long-term average) within the 767–775 ka period (values $> +2\sigma$). This ^{10}Be production enhancement recorded in core MD05-2930 is in phase with the midpoint ^{10}Be production enhancement recorded in core MD90-0961 at 772 ka. It is related to the dipole field collapse linked to the Brunhes/Matuyama (B/M) geomagnetic polarity reversal (labeled GDL s in Figure 5) [e.g., *Valet and Fournier*, 2016]. It coincides with the minimum VADM in PISO-1500 at ~770–775 ka and reasonably agrees with the minimum VADM in SINT-2000 at ~777 ka (Figures 5d and 5e). Its amplitude agrees with the near doubling of the ^{10}Be production rate of the B/M reversal reported from previous ^{10}Be/^{9}Be ratio or ^{10}Be-flux studies of marine sediments [*Raisbeck et al.*, 1985; *Carcaillet et al.*, 2003; *Suganuma et al.*, 2010]. It also agrees with the ^{10}Be production rate increase reported from the EPICA Dome C (EDC) ice core [*Raisbeck et al.*, 2006]. Figures 7c and 7d present the EDC ^{10}Be flux recalculated from raw decay-corrected ^{10}Be concentrations [*Cauquoin et al.*, 2015; *Raisbeck et al.*, 2006] according to the AICC2012 ice age [*Bazin et al.*, 2013] and filtered by using the locally weighted least squares error (Lowess) method. The ^{10}Be overproduction episode recorded in core MD05-2930 is enclosed within the EDC ^{10}Be-flux peak spanning the 766–777 ka interval, while it presents a broader signature in the MD90-0961 core. No ^{10}Be overproduction episode precedes the main signature of the reversal in contradiction with the frequent reporting of a marked RPI low interpreted as a precursor of the B/M reversal (labeled s′ in Figure 5e). This appears also in contradiction with the presence of a ^{10}Be flux peak in the EDC record [*Raisbeck et al.*, 2006] (Figure 7d). However, the anticorrelation between the ^{10}Be-flux and δD in the EDC record [*Raisbeck et al.*, 2006, Figure 1] might suggest that (i) an environmental component might still be prevailing in the ^{10}Be-flux and/or (ii) that it corresponds partially to an artifact due to an underestimation of the EDC accumulation rates from δD [*Cauquoin et al.*, 2015]. Such an anticorrelation is expected for ^{10}Be concentrations because of the inverse relationship between the ^{10}Be dry deposition and snow accumulation rates on the East

Antarctic Plateau, but should be removed in the ^{10}Be-flux term. Moreover, very noisy raw EDC ^{10}Be concentrations characterized by numerous sharp spikes [*Raisbeck et al.*, 2006], together with new geochemical results [*Tison et al.*, 2015], point out that the ^{10}Be peak associated with the "precursor" (Figure 7d) might also partially result from potential ^{10}Be migration within the veins network between large ice crystals, and during fusion recrystallization processes in the extreme bottom layers of ice core [*Landais et al.*, 2004]. These elements cast doubt on the precise geomagnetic interpretation of a precursor at this level in the EDC record. The absence of any strong RPI collapse corresponding to the precursor in the new HINAPIS-1500 stack from North-Atlantic high-sedimentation rate sedimentary cores [*Xuan et al.*, 2016] also questions its strong signature within the PISO-1500 stack [*Channell et al.*, 2009]. Before any conclusion, further studies are required on other sediment series and for other reversals.

5.2. Category 2 ^{10}Be Overproduction Episodes

Interval I is only expressed in core MD05-2930 by a 1.5-fold ^{10}Be/^{9}Be ratio increase centered at 27.5 ka (Figures 5a and 6d). It corresponds with a minor GDL in the PISO-1500 record (Figure 5e). Excursions were documented at 25.5–27 ka in Arctic Ocean sediments [*Nowaczyk and Knies*, 2000] and North Atlantic sediments [*Channell et al.*, 2016]. Considering the age uncertainty, the ^{10}Be overproduction interval (values higher than mean + 1σ; Figure 5c) spanning the 24–32 ka interval could be correlated to the Mono Lake excursion at ~32–34 ka [*Liddicoat and Coe*, 1979; *Wagner et al.*, 2000; *Laj and Channell*, 2015]. This signature, if confirmed, would provide the first cosmogenic evidence obtained from marine sediments of the GDL linked to the Mono Lake excursion, otherwise recognized in the ^{36}Cl signal in the GRIP ice core [*Muscheler et al.*, 2005].

Interval III displays a large ^{10}Be production enhancement between 61 and 65 ka, in phase with GDL a' from the SINT-2000 and PISO-1500 records (Figure 5). The core MD05-2930 is characterized by higher (1.5-fold increase) and long-standing ^{10}Be/^{9}Be ratio interval compared to the 1.4-fold increase ^{10}Be/^{9}Be ratio from core MD05-2920 (Figure 5a). At this age the Norwegian Greenland Sea excursion has been recorded by low intensity and large direction swing in several studies [e.g., *Bleil and Gard*, 1989; *Nowaczyk and Frederichs*, 1999; *Laj et al.*, 2004; *Simon et al.*, 2012; *Nowaczyk et al.*, 1994, 2013]. This cosmogenic overproduction episode was previously documented by *Frank et al.* [1997], *Carcaillet et al.* [2004b], and *Christl et al.* [2010] (Figures 6b and 6c).

Between 95 and 125 ka, intervals IVa and IVb document two successive ^{10}Be/^{9}Be ratio increase episodes (1.2-fold increase) associated with a durable GDL, subdivided into two subunits (GDLs b1 and b2) in the SINT-2000 and PISO-1500 records (Figures 5d and 5e). Low RPI events within this time frame are referred as the post-Blake and Blake events, respectively. Their directional and intensity signatures have been largely documented in many sedimentary records, lava flows, and in a speleothem since the first discovery of the Blake event observed on the Blake Outer Ridge sediment sequences [e.g., *Smith and Foster*, 1969; *Denham*, 1976; *Creer et al.*, 1980; *Tucholka et al.*, 1987; *Tric et al.*, 1991; *Thouveny et al.*, 1990, 2004; *Bourne et al.*, 2012; *Osete et al.*, 2012; *Singer et al.*, 2014]. This long-lasting GDL is also identified by successive large ^{10}Be production enhancements in three studies: the global ^{10}Be-flux stack of *Frank et al.* [1997] (Figure 6a), Portuguese margin [*Carcaillet et al.*, 2004b] (Figure 6b), and ODP Site 983 [*Christl et al.*, 2010] (Figure 6c). The ^{10}Be/^{9}Be ratios of cores MD05-2920 and MD05-2930 present some discrepancies. Interval IVa dated at 98 ka presents a small-amplitude difference (1.3-fold versus 1.2-fold increase). Interval IVb presents significant amplitude differences and timing offsets between both cores. In core MD05-2920, peak IVb is centered at 124 ka and consists in a 1.2-fold increase, while in core MD05-2930 peak IVb points at 119 ka and consists in a 1.4-fold increase. This likely result in an underestimation of the ^{10}Be overproduction episodes associated with the post-Blake and Blake events.

Interval VI documents a significant (1.3-fold) ^{10}Be production signal spanning the 212–217 ka interval (peak at 217 ka). It corresponds to the GDL d in the PISO-1500 record (Figure 5e) that appears as a minor feature in SINT-2000 (Figure 5d). The Pringle Falls excursion has been signaled and dated in the same time interval in sedimentary sequences at Pringle Falls (Oregon) at 218 ± 10 ka [*Herrero-Bervera et al.*, 1994] and at ODP Site 919 (North Atlantic Ocean) between 205 and 225 ka [*Channell*, 2006], in volcanic sequences of Albuquerque Volcanoes (New Mexico) at 211 ± 13 ka [*Singer et al.*, 2008b], and possibly confused with the Mamaku excursion recorded in an ignimbrite of New Zealand dated at 227 ± 8 ka [*McWilliams*, 2001]. This GDL was also documented by ^{10}Be/^{9}Be ratio increases associated with RPI low in the Portuguese margin core

MD95-2040 [*Carcaillet et al.*, 2004b] (Figure 6b) and by high ^{10}Be-flux at ODP Site 1063 [*Christl et al.*, 2010] (Figure 6c).

Interval VIII yields a significant ^{10}Be overproduction episode centered at 286 ka (1.5- and 1.3-fold increases in cores MD05-2920 and MD05-2930, respectively) associated with the GDL g in both SINT-2000 and PISO-1500 (Figures 5d and 5e). This GDL at ~290 ka was recorded as a deep RPI low accompanied by excursional directions in two cores MD95-2039 and MD95-2040 of the Portuguese margin [*Thouveny et al.*, 2004], thus identifying the Portuguese Margin excursion, strongly supported by a large ^{10}Be enhancement [*Carcaillet et al.*, 2004b] (Figure 6b). Several ^{10}Be-flux peaks, with a maximum 1.4-fold increase, are also reported from the EDC record during this time interval [*Cauquoin et al.*, 2015] (Figure 7c).

Interval XI, between 394 and 415 ka, documents two ^{10}Be overproduction episodes (1.3- and 1.2-fold increases, respectively) centered at 406 and 412 ka and associated with the double configuration of GDL i2 documented in PISO-1500 (Figure 5e). This double structure is coherent with repeated RPI minima at 402 and 413 ka in equatorial Pacific sediments [*Valet and Meynadier*, 1993]. Although GDL i consists of a unique low in SINT-2000, the multiple structures of intervals X and XI agree with identification of successive excursions within that time frame: Levantine [*Langereis et al.*, 1997] and 11α/Bermuda [*Lund et al.*, 2001; *Channell et al.*, 2012].

Interval XVII at 582–590 ka reports a 1.3-fold ^{10}Be production enhancement centered at ~586 ka emerging from a massive structure (Figure 5c) associated with GDL n at 590–600 ka in the SINT-2000 and PISO-1500 records. Excursional directions and RPI lows corresponding to this period were described from ODP sites 983 and 984 [*Channell et al.*, 2004] and ODP Leg 172 [*Lund et al.*, 2001]. Other evidences of excursion were reported from lava flows at La Palma (Canary) Island, dated at 602 $\pm$ 24 ka [*Quidelleur et al.*, 1999] and at 580 $\pm$ 8 ka [*Singer et al.*, 2002], and from lava flows of the Eifel (Germany) and from Tahiti, dated at 578 $\pm$ 8 and 579 $\pm$ 6 ka, respectively [*Singer et al.*, 2008a].

Interval XXII corresponds to a ^{10}Be overproduction episode (1.4-fold increase) covering a long-lasting interval in core MD90-0961, peaking at 839 ka. This episode is associated with GDL u in the SINT-2000 and PISO-1500 records and might be related to a geomagnetic instability dated at 822.2 $\pm$ 8.7 ka at La Palma (Canary Islands) [*Singer et al.*, 2002] or to the Kamikastura excursion recorded in Icelandic lavas and dated at 862 $\pm$ 51 ka [*Camps et al.*, 2011].

5.3. Category 3 ^{10}Be Production Episodes

This third category includes minor ^{10}Be production episodes that emerge slightly over the long-term average ^{10}Be/^{9}Be ratio ($<1\sigma$). Some of those episodes have been labeled and briefly described if recorded in both cores and related to well-defined GDL in SINT-2000 and PISO-1500.

Interval IX documents several minor ^{10}Be overproduction episodes corresponding to GDL h characterized by a double GDL minimum in PISO-1500 (Figure 5e). Core MD05-2920 presents a similar structure with two distinct peaks (1.3- and 1.1-fold increases) centered at ~310 and ~327 ka, respectively. The ^{10}Be/^{9}Be ratio signature of core MD05-2930 presents a rather massive interval of enhanced ^{10}Be production (1.1-fold increase) with smaller peaks centered at 312, 319, and 327 ka. Two ^{10}Be-flux peaks (1.3-fold increase) have also been identified during that time interval (307 ka, 320–330 ka) in the EDC record [*Cauquoin et al.*, 2015] (Figure 7c).

Interval X yields several increasing ^{10}Be-production intervals (~1.2-fold increase) within the 367–383 ka period in cores MD05-2920 and MD05-2930 and might be associated with GDL i1 from the PISO-1500 record.

The timing of intervals IX and X is consistent with excursions reported within the 310–330 ka and 360–420 ka intervals at several marine sediment sites [*Langereis et al.*, 1997; *Lund et al.*, 2001; *Channell et al.*, 2012].

Interval XII displays two ^{10}Be production enhancements (1.1- and 1.2-fold increases) at 438 and 447 ka, respectively. These twin peaks might be related to the double structure of GDL j in PISO-1500 (j1 at 430–445 ka and j2 at 455–460 ka), instead of a single GDL j, as reported in SINT-2000.

Interval XIII centered at 490–500 ka is barely significant with only a maximum 1.0-fold ^{10}Be/^{9}Be ratio increase, but it correlates with GDL k, a wide GDL of small amplitude in SINT-2000 and a narrow GDL of large amplitude in PISO-1500.

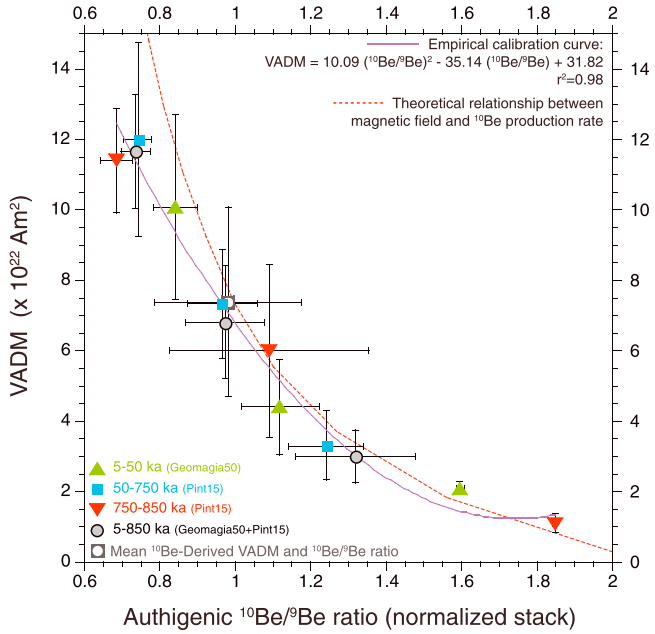

Figure 8. Calibration of the normalized authigenic $^{10}Be/^{9}Be$ ratio stack using absolute values of the virtual axial dipole moment (VADM) extracted from the Geomagia50.v3 [*Brown et al.*, 2015a, 2015b] and PINT2015-05 [*Biggin et al.*, 2009] databases. Average VADM and authigenic $^{10}Be/^{9}Be$ ratio values are computed for different clusters (see text and Table S6 for details). Associated error bars correspond to the standard deviation of the values used in each cluster. The polynomial fit (purple line) between these calibration points is used to compute the ^{10}Be-derived GDM presented in Figures 9 and 10. The dotted red line represents the theoretical relationship between the relative strength of the magnetic field and ^{10}Be cosmogenic nuclide production rate according to model from *Masarik and Beer* [1999, 2009] and *Wagner et al.* [2000].

Intervals XIV and XVI yield two ^{10}Be production increase episodes centered at 523 and 550 ka, respectively. These episodes are associated with the category 1 ^{10}Be overproduction interval XV (see above).

Interval XVIII documents a 1.2-fold ^{10}Be production increase centered at 615 ka and associated with GDL o in the PISO-1500 record. Evidences of an excursion corresponding to this period arise from anomalous directions in the Lishi loess sequence [*Liu et al.*, 1988] and from La Palma (15β)/West Eifel 2 [*Lund et al.*, 2006; *Singer et al.*, 2008a].

Interval XIX reports a small ^{10}Be overproduction episode between 690 and 704 ka with a maximum peak at 700 ka (1.2-fold increase). This large interval is the "tip of an iceberg" that mirrors the large GDLs p and q structure present in both SINT-2000 and PISO-1500 records (Figures 5d and 5e). The interval XIX can also be related to a double inclination anomaly recorded in sediments deposited during MIS 17 in Osaka Bay [*Biswas et al.*, 1999].

The interval XX at 715–730 ka is hardly significant, documenting a 0.9-fold $^{10}Be/^{9}Be$ ratio increases centered at 715 and 729 ka in cores MD05-2930 and MD90-0961, respectively. The chronological offset of this interval between the two records likely explains some over smoothing at this level where GDL r is recorded at 730 ka (Figure 5).

Two minor $^{10}Be/^{9}Be$ ratio increase episodes deserve additional analyses before labeling: they include two peaks coherent with the Albuquerque and Mamaku excursions centered at 153 ka and 240 ka [*Peate et al.*, 1996; *Shane et al.*, 1994], respectively. The Albuquerque event is expressed solely in core MD05-2930 and is not put forth by a clear GDL in the SINT-2000 and PISO-1500 records. The Mamaku event corresponds to a $^{10}Be/^{9}Be$ ratio increase (1.2-fold), but its age deviates in both cores (232 and 240 ka in core MD05-2930 and MD05-2920, respectively). A slight alignment of both peaks by 4 ka (Figure 5a) would be coherent with a ^{10}Be production enhancement at ~236 ka in core MD95-2040 from the Portuguese Margin (Figure 6b) [*Carcaillet et al.*, 2004b] corresponding to GDL e from the PISO-1500 record (Figure 5e). This would also agree with the age of 230 ± 12 ka obtained on excursional lava flows at Mamaku (New Zealand) [*Shane et al.*, 1994].

6. ^{10}Be-Derived Virtual Dipole Moments

Since atmospheric cosmogenic ^{10}Be production rates are modulated at global scale by the geomagnetic dipole moment (GDM) (Figure 5), empirical and theoretical arguments [e.g., *Lal and Peters*, 1967; *Masarik and Beer*, 2009] can be used to calibrate the $^{10}Be/^{9}Be$ ratio by using absolute virtual (or virtual axial) dipole moment values (i.e., VDM or VADM) in order to reconstruct a ^{10}Be-derived geomagnetic dipole moment record (Figures 8 and 9). Absolute GDM values were extracted from absolute paleointensity databases: Geomagia50.v3 (http://geomagia.gfz-potsdam.de, December 2015) [*Brown et al.*, 2015a, 2015b] and PINT2015-05 (http://earth.liv.ac.uk/pint/, December 2015) [*Biggin et al.*, 2009]. Reliability criteria were used

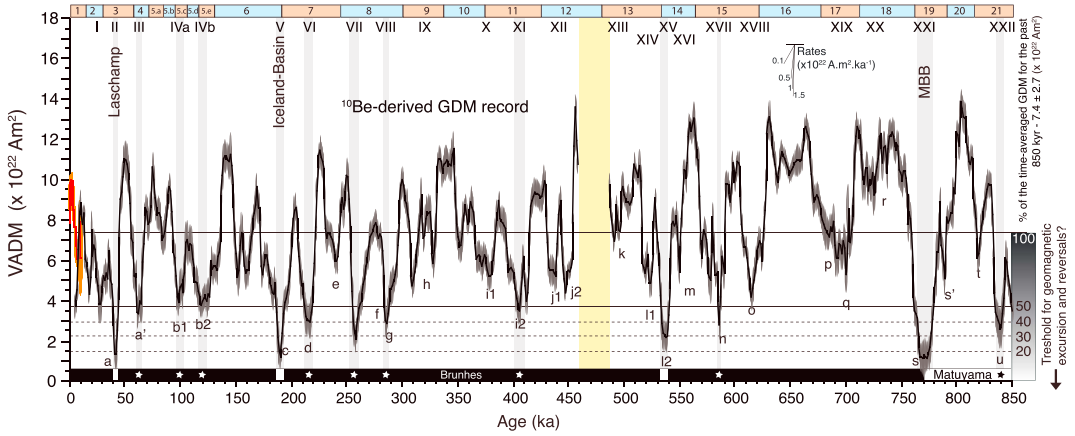

Figure 9. ^{10}Be-derived GDM reconstruction of the 5–850 ka interval. From 0 to 10 ka, the red line is the global field model CALS10k.1b [*Korte et al.*, 2011]. The ^{10}Be/^{9}Be ratio increase intervals are highlighted by vertical grey bands and numbered from I to XXII, adapted from the labeling of *Carcaillet et al.* [2004a] and *Ménabréaz et al.* [2014]. Geomagnetic dipole lows (GDLs) are labeled a to u. VADM rates of changes (x 10^{22} Am^2 ka^{-1}) are shown. Field threshold percentages are calculated versus the time-averaged GDM for the past 850 ka ($7.4 \pm 2.7 \times 10^{22}$ Am^2). The Laschamp (II), Iceland Basin (V), and MBB (XXI) present field value percentages below 20%, while the other major events—VII and XV—are below a 30% threshold. Secondary ^{10}Be-production episodes are found below ~50% of the average field value (~3.7×10^{22} Am^2). The yellow band underlines the disturb interval excluded for geomagnetic interpretation.

for selection. They include (i) quality of methods and number of samples used to produce the paleointensity (PI) values, (ii) the presence of suitable paleomagnetic direction information, and (iii) a reasonable error bar on the age. Only PI data provided with standard deviation and age errors lower than 10% were retained: a total of 487 absolute VDM or VADM data (~30% of the total data set) are available for our calibration procedure (Figure 10d). This selection allows excluding extreme values that arise from distinct measurement procedures and/or that does not provide sufficient confidence (these values are represented by open circle in Figure 10d). After this first data filtering, we have associated clusters of high, intermediate, and low GDM values with clusters of low, medium, and high values of the ^{10}Be/^{9}Be ratio stack within four distinct time intervals following the procedure used by *Ménabréaz et al.* [2012, 2014] in order to account for uncertainties inherent to volcanic paleomagnetic data and to their nonuniform distribution through time. For each time interval, average values are calculated to discriminate the data in three clusters defined as data lower than mean $\pm 1\sigma$, data comprised between mean -1σ and mean $+1\sigma$, and data higher than mean $\pm 1\sigma$ limits (see Table S6).

For the first time interval, data are restricted to the 5 to 50 ka including the Laschamp excursion and are compared with data extracted from the Geomagia50.v3 database. This interval has an average absolute GDM value of $4.97 \pm 2.43 \times 10^{22}$ Am^2 and an average ^{10}Be/^{9}Be ratio value of $1.09 \pm 0.18 \times 10^{-8}$. The second time interval—i.e., 50–750 ka—excludes the Laschamp excursion and the Brunhes-Matuyama reversal periods. This interval has an average absolute GDM of $7.43 \pm 2.87 \times 10^{22}$ Am^2 and an average ^{10}Be/^{9}Be ratio value of $0.96 \pm 0.17 \times 10^{-8}$. The third time interval, 750–850 ka, includes the Brunhes-Matuyama reversal and has an average absolute GDM of $6.50 \pm 3.42 \times 10^{22}$ Am^2 and an average ^{10}Be/^{9}Be ratio value of $1.05 \pm 0.30 \times 10^{-8}$. Finally, the whole time interval 5–850 ka was considered with an average absolute GDM of $6.90 \pm 2.97 \times 10^{22}$ Am^2 and an average authigenic ^{10}Be/^{9}Be ratio value of $0.98 \pm 0.20 \times 10^{-8}$.

All clusters computed for all time intervals are used to define an empirical calibration curve by polynomial regression through all calibration points (Figure 8). As raised by *Ménabréaz et al.* [2014], the calculation of arithmetic means inside the clusters introduces slight errors given the nonlinear relationship between geomagnetic field variation and ^{10}Be production rate. These errors are included in the 2σ uncertainty associated with the ^{10}Be-derived GDM record presented in Figures 9 and 10 (Table S7). The used polynomial regression is in good agreement with the theoretical relationship established by *Masarik and Beer* [1999, 2009] between the magnetic field strength and ^{10}Be cosmogenic nuclide production rate (Figure 8).

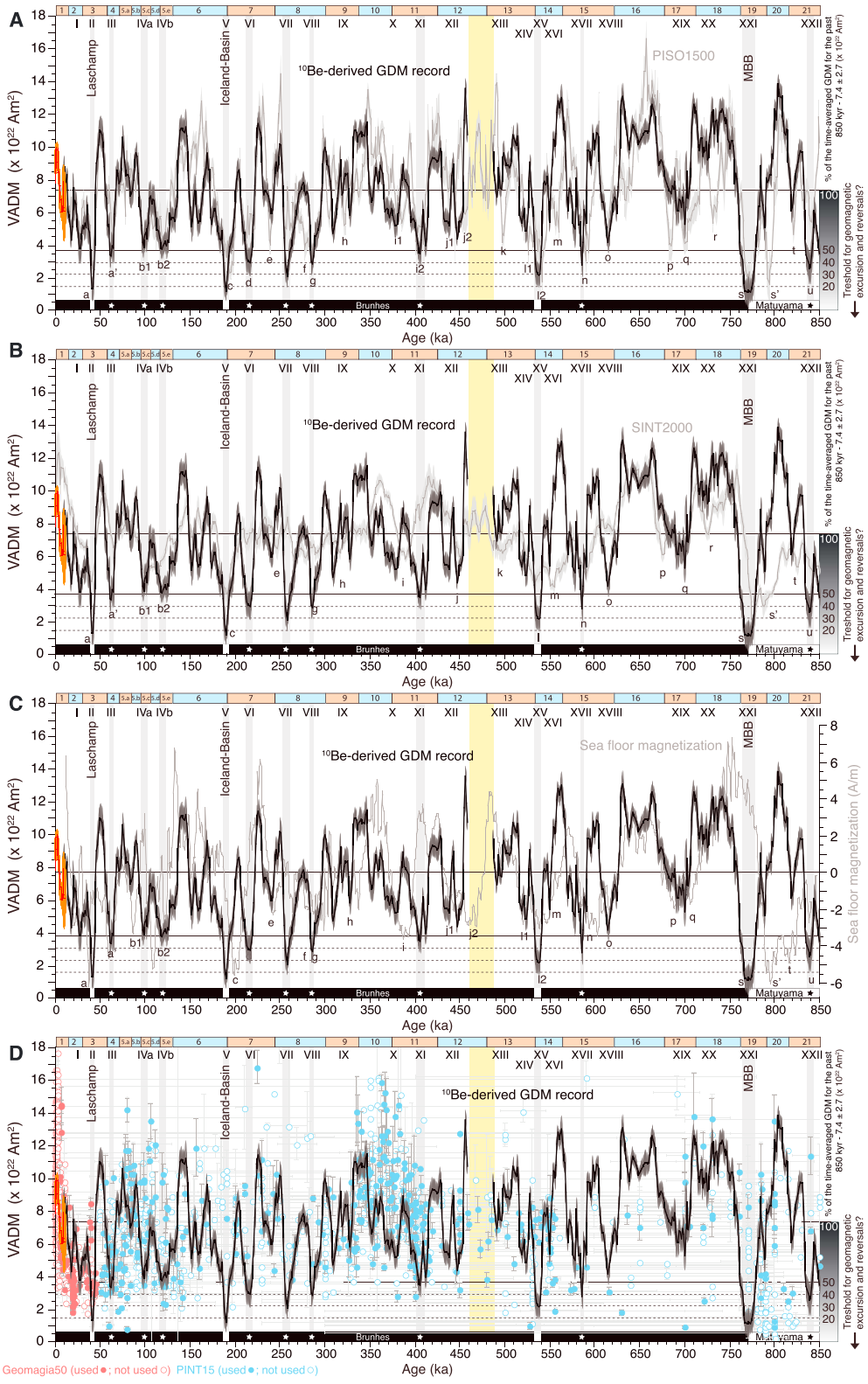

Figure 10. ^{10}Be-derived GDM for the 5–850 ka interval (black) compared to (a) the PISO-1500 VADM record [*Channell et al.*, 2009], (b) the SINT-2000 VADM record [*Valet et al.*, 2005], (c) the southeast Pacific deep-sea floor magnetization record [*Gee et al.*, 2000], and (d) the absolute intensity from the Geomagia50.v3 [*Brown et al.*, 2015a, 2015b] and PINT2015-05 database [*Biggin et al.*, 2009]. The full dots were used for the ^{10}Be-GDM calibration; the empty circles were excluded (see text for details). All records are plotted on their respective time scales.

7. Discussion

7.1. ^{10}Be-Derived GDM Variations

Dipole moment values of the ^{10}Be-derived GDM record range from 1.15 to 13.90×10^{22} Am^2 around an average value and standard deviation of $7.4 \pm 2.7 \times 10^{22}$ Am^2 (Figure 9 and Table S7). The mean value of the standard error associated with the stack is 0.73 Am^2. The average ^{10}Be-derived GDM value is remarkably consistent with the long-time average values of $7.3 \pm 1.8 \times 10^{22}$ Am^2 and $7.5 \pm 2.6 \times 10^{22}$ Am^2 computed for the last 850 ka from PISO-1500 and SINT-2000, respectively [*Channell et al.*, 2009; *Valet et al.*, 2005] (Figures 10a and 10b). These values are not significantly different from the long-term VADM or VDM averages computed from the PADM2M ($6.2 \pm 1.2 \times 10^{22}$ Am^2) [*Ziegler et al.*, 2011] and from the absolute PI data set used for calibration ($6.9 \pm 3.0 \times 10^{22}$ Am^2) (Figure 10d). The average VADM value is also relatively similar with the present dipole moment value (7.78×10^{22} Am^2). In Figure 9, the ^{10}Be-derived GDM record is completed by a 2 ka overlap with the global field model CALS10k.1b [*Korte et al.*, 2011]. The lack of correlation of ^{10}Be-derived GDM record with archeomagnetic VADM reconstruction between 5 and 8 ka could be attributed to disturbed sediments at the MD05-2930 core top resulting from coring processes (similar weakly constrain recent field behaviors are often observed in RPI data from piston cores) together with low global coverage and, especially, large disparity of the absolute intensity data from that period (Figure 10d). Our new ^{10}Be-derived GDM record presents strong compatibilities with published VADM stacks, despite slight age offsets (i.e., at 330–350 ka, 550–570 ka, and 710–720 ka) (Figures 10a and 10b) that may result from various causes (e.g., age model uncertainties and pDRM lock-in effects in RPI curves). Moreover, this new record agrees with the southeast Pacific seafloor magnetization record obtained from deep-towed magnetometry [*Gee et al.*, 2000], thus confirming their common dipolar geomagnetic moment origin (Figure 10c).

The compatibility of the ^{10}Be-derived GDM with paleomagnetic reference curves based on several distinct approaches and calibration procedures supports a posteriori the reliability of principles and methods of the reconstruction of geomagnetic dipole moment variations by using cosmogenic nuclide production. Therefore, this record provides an independent way to evaluate critical GDM values, change rates, and thresholds linked to large-amplitude geomagnetic field changes such as excursions and reversals. The chronology of the record based on the astronomically calibrated LR04 stack yields an updated time series of GDL linked to Brunhes excursions and B/M reversal, which provides a helpful template for discussing specifically each geomagnetic events by using complementary techniques such as paleomagnetic measurements and ^{40}Ar/^{39}Ar dating on lava flows.

7.2. Geomagnetic Dipole Low (GDL) Frequency

Our results confirm that GDLs, correlated or not with reported excursions, are intrinsic features of the geodynamo behavior, reflecting its instability, and triggering mechanisms that may also generate polarity reversals [*Laj and Channell*, 2015]. The future analyses of frequency, timing, amplitude, and rates of geomagnetic instabilities seen from the cosmogenic perspective will provide critical constraints, complementary of paleomagnetic reconstructions, to feed and assess the validity of numerical and analogic dynamo models [*Busse*, 1978; *Vanyo et al.*, 1995; *Olson et al.*, 2010]. One striking features observed in Figure 9 is the apparent variation of GDL density across the Brunhes Chron. From 8 to 300 ka, nine major GDLs are associated with significant ^{10}Be overproduction episodes, while between 301 and 775 ka only three of those significant GDLs are observed. This suggests an increase in GDL frequency associated with recognized excursions between the early Brunhes and the late Brunhes phase. The average GDM value of the 8–300 ka interval ($6.4 \pm 2.3 \times 10^{22}$ Am^2) is lower than that of the 301–775 ka interval ($8.1 \pm 2.6 \times 10^{22}$ Am^2), which is coherent with a reciprocal relationship between the number of GDL, their length, and the average value of the dipole moment. A similar GDM distinction is found when excluding the major GDLs from the calculation: $7.0 \pm 1.9 \times 10^{22}$ and $8.4 \pm 2.3 \times 10^{22}$ Am^2 for the 8–300 ka and 301–775 ka intervals, respectively. These calculations give an identical ~20% lower average dipole moment for the 8–300 ka interval compared to the 301–775 ka first half of the Brunhes chron (Figure 9). This implies that (i) a fairly weak GDM triggers, or is triggered by, frequent and/or durable instabilities (GDL and excursions), and on the contrary (ii) a strong GDM triggers, or is triggered by, a low frequency of instabilities (few GDL and excursions).

This observation favors the hypothesis that the geodynamo becomes periodically unstable when the dipole field is weak [e.g., *Singer et al.*, 2008b; *Olson et al.*, 2010] and tends to reject the hypothesis of pure stochastic unstabilities of the geodynamo [*Zhang and Gubbins*, 2000].

7.3. GDL Thresholds for ^{10}Be Overproduction Episodes

As ^{10}Be production at millennial scale is solely associated with the geomagnetic dipole moment modulation, only GDM drops can support the overproduction episodes. A critical value for triggering excursions or reversals was assessed by *Channell et al.* [2009] at ~2.5×10^{22} Am^2, representing about 30% of the present dipole moment value. All category 1 ^{10}Be overproduction episodes, including the fourth largest excursions (i.e., Laschamp, Iceland Basin, Calabrian Ridge 0, and Big Lost) and the B/M reversal, result from such events and provide such low calibrated ^{10}Be-derived GDM values (Figure 9). The B/M reversal and the Laschamp excursion present the weakest GDM values of 1.2 and 1.4×10^{22} Am^2, respectively. This is equivalent to less than 20% of the mean average GDM over the period (Figure 9). The Iceland Basin excursion yields a GDM value of 1.6×10^{22} Am^2 (~22%), while two other events—Calabrian Ridge 0 and Big Lost—present GDM values of 2.1×10^{22} Am^2 (29% of the mean GDM). The somehow lower ^{10}Be/^{9}Be ratio peaks of these last two events that hardly exceed the $+2\sigma$ limit of category 1 events supposed that they might be related to the upper limit of the category 2 ^{10}Be overproduction episodes rather than being associated with the others three GDL maxima. All secondary Brunhes excursions of category 2 ^{10}Be overproduction episodes correspond with GDM values below $3.3–3.9 \times 10^{22}$ Am^2 (45 to 52%) of the mean GDM.

Such observations may help to understand the GDM thresholds necessary to trigger geomagnetic excursions and/or reversals [e.g., *Laj and Channell*, 2015; *Valet and Fournier*, 2016]. A threshold at 50% of the present GDM is evidenced since each ^{10}Be-derived GDM values lower than this limit are associated with paleomagnetic excursions, i.e., a directional instability largely overpassing the limits of secular variation. The B/M reversal, the Laschamp excursion, and Iceland Basin excursion, often considered as transient full reversals, (and marked as such in the ocean floor anomaly record (Figure 10c)) occurred below a GDM of 1.6×10^{22} Am^2, i.e., ~20% of the present GDM value. Therefore, the threshold of 50% of the actual GDM would suffice to trigger category 2 excursions, while the critical threshold of 20 to 30% seems to be required to trigger category 1 excursions and/or reversals.

7.4. GDL Durations and Decay/Recovery Rates

In order to compare the field features of the last reversal versus the largest Brunhes excursions, defined by category 1 ^{10}Be overproduction episodes, we derived the GDM decay/recovery rates from our record. These rates represent the best relative estimates considering the resolution and uncertainty associated with our record. Although they can be discussed due to forthcoming improvements in their accuracy and precision, the strong compatibilities of our record with RPI stacks support the proposed approach. Furthermore, the occurrence of systematic uncertainty changes between specific events, or between the decay or recovery phases, is hardly possible, which makes their comparison relevant. We calculated these rates for two types of GDL durations: 5 and 10 ka to test possible disparities. Computed average decay rates for the 5 and 10 ka intervals are 0.9 ± 0.5 and $0.6 \pm 0.2 \times 10^{22}$ Am^2 ka^{-1}, while their mean average recovery rates are 0.8 ± 0.3 and $0.5 \pm 0.2 \times 10^{22}$ Am^2 ka^{-1}, respectively. These coherent results suggest an increase of the decay/recovery rates in the 5 ka before and 5 ka after the major event peak (Figure 9). Maximum rates concern the Laschamp excursion with 1.5×10^{22} Am^2 ka^{-1} for the decay and 0.9×10^{22} Am^2 ka^{-1} for the recovery. Similar decay rates have been calculated for the Laschamp excursion from ice core records [*Wagner et al.*, 2000; *Muscheler et al.*, 2005], from the high-resolution GLOPIS record [*Laj et al.*, 2004], and from the ^{10}Be derived GDM global stack by *Ménabréaz et al.* [2012]. Lower decay and recovery rates are computed for the B/M transition, associated with the 8 ka duration of the low-intensity interval (Table 1). Change rates computed on longer term, over $\pm$30 ka before and after the B/M transition between the GDM minimum and surrounding GDM maxima, are 0.36×10^{22} Am^2 ka^{-1} for the decay and 0.42×10^{22} Am^2 ka^{-1} for the recovery. The same computation for the Laschamp excursion gives 1.1 and 0.9×10^{22} Am^2 ka^{-1} for the 41–50 and 35–41 ka intervals. The decay and recovery rates for all events present a small asymmetric feature with consistently higher decay rates of about 25–40% compared to recovery rates, although important variation between the events is revealed by large standard deviations. By contrast, the change rates of the B/M transition are lower for the decay than for the recovery for all calculation methods. Independently, from the time window selected for calculating the decay/recovery rates, the results of this study suggest lower change rates for the B/M transition compared to major excursions/events. This observation suggests that geodynamo behaviors are different for excursions/events and reversal. If confirmed our

observation would support the *Gubbins* [1999] hypothesis that excursions reflect relatively rapid and short-lived reversal of the field generated by flow of liquid in the outer core, while reversal involve longer-term deeper processes of geomagnetic field generation and interactions with the inner core induced field. According to that model, excursions could not stand longer than 3 ka, while reversals would span longer time intervals. Our study shows that all major GDL associated with the Laschamp, Iceland Basin, Calabrian Ridge 0, and Big Lost events (i.e., II, V, VII, and XV) lasted less than 3 ka, while the episode associated with the B/M transition lasted 8 ka (Table 1). The case of category 2 GDLs is less clear: they are characterized by a large range of duration (1 to 7 ka), likely related to a weaker definition of ^{10}Be overproduction episode limits on the stack record. Further investigations on this record associated with paleomagnetic measurements, as well as other higher-resolution ^{10}Be cosmogenic analyses of new records globally distributed, are currently underway to refine field behavior systematics.

Finally, it is interesting to compare the minimum and maximum decay rates computed from our long-term GDM variation study during the Brunhes Chron (0.4 and 1.5×10^{22} Am^2 ka^{-1}) with the decay rate computed from archeomagnetic results that shows an acceleration for the last millennia (3×10^{22} Am^2 ka^{-1}) [*Genevey et al*., 2003; *Gallet et al*., 2014].

8. Conclusions

The authigenic ^{10}Be/^{9}Be ratio records obtained from low-latitude cores MD05-2920, MD05-2930, and MD90-0961 reveal the variation of the atmospheric ^{10}Be global production rate between 5 and 850 ka. Correlation of the δ^{18}O records with the standard LR04 stack enables the setting of a robust chronology, allowing comparison with paleomagnetic stacked records of the virtual axial dipole moment obtained from sediments and lavas, as well as with the southeast equatorial Pacific seafloor magnetic anomalies series. These comparisons confirm that significant ^{10}Be enhancements are chronologically related with the global occurrence of geomagnetic dipole lows. A first category of ^{10}Be overproduction episodes corresponds to major geomagnetic dipole lows associated with well-known paleomagnetic excursions (Laschamp, Iceland-Basin, Calabrian Ridge 0, and Big Lost) and with the Brunhes-Matuyama transition. Weaker ^{10}Be overproduction episodes are associated with minor geomagnetic dipole lows associated with less constrained paleomagnetic excursions. The calibration of the ^{10}Be/^{9}Be ratio stacked record using virtual dipole moment values extracted from absolute paleointensities drawn from the PINT and Geomagia databases is supported by the nonlinear relationship empirically established between ^{10}Be production and virtual axial dipole moment values, and its compatibility with the production models. The ^{10}Be-derived geomagnetic dipole moment record covering the Brunhes Chron and the Brunhes-Matuyama transition is in general agreement with sedimentary paleomagnetic stacks (namely with the PISO-1500 stack). It allows to assess characteristic critical states of the dipole moment that triggered either excursion types 1 and 2, or reversals. A critical threshold of ~4×10^{22} Am^2 (50% of the current virtual dipole moment) triggers category 2 excursions, while dipole moment values below 2×10^{22} Am^2 trigger category 1 excursions, or reversals. All category 1 ^{10}Be overproduction episodes are associated with geomagnetic dipole lows linked to geomagnetic excursions that have durations below 3 ka, while the episode associated with the Brunhes-Matuyama transition spans a longer (8 ka) time interval. A possible influence of the average dipole moment value on the occurrence of geomagnetic dipole lows is suggested by different mean dipole moment values computed for different time intervals: the 8–300 ka interval with a mean of $7.0 \pm 1.9 \times 10^{22}$ Am^2 is characterized by more frequent dipole lows than the 301–775 ka interval with a mean of $8.4 \pm 2.3 \times 10^{22}$ Am^2. This study provides new insight on the long-term geodynamo variation with robust information on amplitudes and timing of geomagnetic dipole moment. The pacing, duration, and change rates characterizing geomagnetic dipole lows reported in this study provide new constraints for geodynamo models.

Acknowledgments
The authors particularly want to acknowledge contributions of colleagues from CEREGE: Kazuyo Tachikawa for radiocarbon calibrations, Laurence Vidal for discussing δ^{18}O records, Mélanie Baroni for her advice with ^{10}Be data processing in ice core, and Mireille Perrin for her help in the filtering strategy applied to absolute VDM data sets. We also want to thank J.E.T. Channell and an anonymous reviewer for their constructive and helpful comments. Special thanks are due to the ASTER Team (Maurice Arnold, Georges Aumaitre, and Karim Keddadouche) for the ^{10}Be measurements performed at the ASTER AMS national facility (CEREGE, Aix-en-Provence). This equipment is supported by the INSU/CNRS, the IRD, and by the ANR through the program "EQUIPEX Investissement d'Avenir." This study is a main contribution of the project MAGORB (ANR 09 BLAN 0053) and was completed with the support of the ERC advanced grant GA 339899-EDIFICE under the ERC's 7th Framework Program (FP7-IDEA-ERC). The data presented in this study are available within the supporting information.

References

Anderson, R. F., Y. Lao, W. S. Broecker, S. E. Trumbore, H. J. Hofmann, and W. Wolfli (1990), Boundary scavenging in the Pacific Ocean: A comparison of ^{10}Be and ^{231}Pa, *Earth Planet. Sci. Lett.*, *96*, 287–304.

Arnold, M., M. Silke, D. L. Bourlès, R. Braucher, L. Benedetti, R. C. Finkel, G. Aumaître, A. Gottdang, and M. Klein (2010), The French accelerator mass spectrometry facility ASTER: Improved performance and developments, *Nucl. Instrum. Methods Phys. Res. B*, *268*, 1954–1959, doi:10.1016/j.nimb.2010.02.107.

Baroni, M., E. Bard, J. R. Petit, O. Magand, and D. L. Bourlès (2011), Volcanic and solar activity, and atmospheric circulation influences on cosmogenic ^{10}Be fallout at Vostok and Concordia (Antarctica) over the last 60 years, *Geochim. Cosmochim. Acta*, *75*(22), 7132–7145, doi:10.1016/j.gca.2011.09.002.

Bassinot, F. C., L. D. Labeyrie, E. Vincent, X. Quidelleur, N. J. Shackleton, and Y. Lancelot (1994), The astronomical theory of climate and the age of the Brunhes–Matuyama magnetic reversal, *Earth Planet. Sci. Lett.*, *126*, 91–108.

Bazin, L., et al. (2013), An optimized multi-proxy, multi-site Antarctic ice and gas orbital chronology (AICC2012): 120–800 ka, *Clim. Past*, *9*, 1715–1731, doi:10.5194/cp-9-1715-2013.

Beaufort, L., Chen, M.-T., Droxler, A. W., and the Shipboard Scientific Party (2005), MD148/PECTEN-IMAGES XIII cruise report, Inst. Polaire Fr. Paul Emile Victor, Brest, France.

Beer, J., et al. (1990), Use of ^{10}Be in polar ice to trace the 11-year cycle of solar activity, *Nature*, *347*(6289), 164–166, doi:10.1038/347164a0.

Biggin, A. J., G. Strik, and C. G. Langereis (2009), The intensity of the geomagnetic field in the late-Archaean: New measurements and an analysis of the updated IAGA palaeointensity database, *Earth Planets Space*, *61*(1), 9–22.

Biswas, D. K., M. Hyodo, and Y. Tanigucchi (1999), Magnetostratigraphy of Pio-Pleistocene sediments in a 1700 m core from Osaka Bay, Southwestern Japan and short geomagnetic events in the middle Matuyama and the early Brunhes chrons, *Palaeogeogr. Palaeoclimatol. Palaeoecol.*, *148*, 233–248.

Bleil, U., and G. Gard (1989), Chronology and correlation of quaternary magnetostratigraphy and nannofossil biostratigraphy in Norwegian–Greenland sea sediments, *Geol. Rundsch.*, *78*, 1173–1187.

Bourlès, D. L., G. M. Raisbeck, and F. Yiou (1989), ^{10}Be and ^{9}Be in marine sediments and their potential for dating, *Geochim. Cosmochim. Acta*, *53*(2), 443–452.

Bourne, M., C. Mac Niocaill, A. L. Thomas, M. F. Knudsen, and G. M. Henderson (2012), Rapid directional changes associated with a 6.5 kyr-long Blake geomagnetic excursion at the Blake–Bahama Outer Ridge, *Earth Planet. Sci. Lett.*, *333*, 31–34.

Brown, E. T., C. I. Measures, J. M. Edmond, D. L. Bourlès, G. M. Raisbeck, and F. Yiou (1992), Continental inputs of beryllium to the oceans, *Earth Planet. Sci. Lett.*, *114*(1), 101–111.

Brown, M. C., F. Donadini, M. Korte, A. Nilsson, K. Korhonen, A. Lodge, S. N. Lengyel, and C. G. Constable (2015a), GEOMAGIA50.v3: 1. General structure and modifications to the archeological and volcanic database, *Earth Planets Space*, *67*, 83, doi:10.1186/s40623-015-0232-0.

Brown, M. C., F. Donadini, A. Nilsson, S. Panovska, U. Frank, K. Korhonen, M. Schuberth, M. Korte, and C. G. Constable (2015b), GEOMAGIA50.v3: 2. A new paleomagnetic database for lake and marine sediments, *Earth Planets Space*, *67*, 70, doi:10.1186/s40623-015-0233-z.

Busse, F. H. (1978), Magnetohydrodynamics of the Earth's dynamo, *Annu. Rev. Fluid Mech.*, *10*, 435–462, doi:10.1146/annurev.fl.10.010178.002251.

Camps, P., B. S. Singer, C. Carvallo, A. Goguitchaichvili, G. Fanjat, and B. Allen (2011), The Kamikatsura event and the Matuyama–Brunhes reversal recorded in lavas from Tjörnes Peninsula, northern Iceland, *Earth Planet. Sci. Lett.*, *310*, 33–44.

Carcaillet, J. T., Thouveny, N., and D. L. Bourlès (2003), Geomagnetic moment instability between 0.6 and 1.3 Ma from cosmonuclide evidence, *Geophys. Res. Lett.*, *30*(15), 1792, doi:10.1029/2003GL017550.

Carcaillet, J. T., D. L. Bourlès, and N. Thouveny (2004a), Geomagnetic dipole moment and ^{10}Be production rate intercalibration from authigenic ^{10}Be/^{9}Be for the last 1.3 Ma, *Geochem. Geophys. Geosyst.*, *5*, Q05006, doi:10.1029/2003GC000641.

Carcaillet, J. T., D. L. Bourlès, N. Thouveny, and M. Arnold (2004b), A high resolution authigenic 10Be/9Be record of geomagnetic moment variations over the last 300 ka from sedimentary cores of the Portuguese margin, *Earth Planet. Sci. Lett.*, *219*(3), 397–412, doi:10.1016/S0012821X03007027.

Cauquoin, A., A. Landais, G. M. Raisbeck, J. Jouzel, L. Bazin, M. Kageyama, J.-Y. Peterschmitt, M. Werner, E. Bard, and ASTER Team (2015), Comparing past accumulation rate reconstructions in East Antarctic ice cores using ^{10}Be, water isotopes and CMIP5-PMIP3 models, *Clim. Past*, *11*, 355–367, doi:10.5194/cp-11-355-2015.

Champion, D., M. Lanphere, and M. Kuntz (1988), Evidence for a new geomagnetic reversal from lava flows in Idaho: Discussion of short polarity reversals in the Brunhes and late Matuyama polarity chrons, *J. Geophys. Res.*, *93*, 11,667–11,680, doi:10.1029/88JB03323.

Channell, J. E. T. (1999), Geomagnetic paleointensity and directional secular variation at Ocean Drilling Program (ODP) Site 984 (Bjorn Drift) since 500 ka: Comparisons with ODP Site 983 (Gardar Drift), *J. Geophys. Res.*, *104*, 22,937–22,951, doi:10.1029/1999JB900223.

Channell, J. E. T. (2006), Late Brunhes polarity excursions (Mono Lake, Laschamp, Iceland Basin and Pringle falls) recorded at ODP site 9191 (Irminger Basin), *Earth Planet. Sci. Lett.*, *244*, 378–393.

Channell, J. E. T. (2014), The Iceland Basin excursion: Age, duration, and excursion field geometry, *Geochem. Geophys. Geosyst.*, *15*, 4920–4935, doi:10.1002/2014GC005564.

Channell, J. E. T., D. A. Hodell, and B. Lehman (1997), Relative geomagnetic paleointensity and d18O at ODP Site 983 (Gardar Drift, north Atlantic) since 350 ka, *Earth Planet. Sci. Lett.*, *153*, 103–118.

Channell, J. E. T., J. H. Curtis, and B. P. Flower (2004), The Matuyama–Brunhes boundary interval (500–900 ka) in North Atlantic drift sediments, *Geophys. J. Int.*, *158*, 489–505.

Channell, J. E. T., C. Xuan, and D. A. Hodell (2009), Stacking paleointensity and oxygen isotope data for the last 1.5 Myr (PISO-1500), *Earth Planet. Sci. Lett.*, *283*(1–4), 14–23, doi:10.1016/j.epsl.2009.03.012.

Channell, J. E. T., D. A. Hodell, and J. H. Curtis (2012), ODP Site 1063 (Bermuda Rise) revisited: Oxygen isotopes, excursions and paleointensity in the Brunhes Chron, *Geochem. Geophys. Geosyst.*, *13*, Q02001, doi:10.1029/2011GC003897.

Channell, J. E. T., R. J. Harrison, I. Lascu, I. N. McCave, F. D. Hibbert, and W. E. N. Austin (2016), Magnetic record of deglaciation using FORC-PCA, sortable-silt grain size, and magnetic excursion at 26 ka, from the Rockall Trough (NE Atlantic), *Geochem. Geophys. Geosyst.*, *17*, 1823–1841, doi:10.1002/2016GC006300.

Chase, Z., R. F. Anderson, M. Q. Fleisher, and P. W. Kubik (2002), The influence of particle composition and particle flux on scavenging of Th, Pa and Be in the ocean, *Earth Planet. Sci. Lett.*, *204*(1), 215–229.

Chmeleff, J., F. von Blanckenburg, K. Kossert, and D. Jakob (2010), Determination of the ^{10}Be half-life by multicollector ICP-MS and liquid scintillation counting, *Nucl. Instrum. Methods Phys. Res. B.*, *268*(2), 192–199, doi:10.1016/j.nimb.2009.09.012.

Christl, M., J. Lippold, F. Steinhilber, F. Bernsdorff, and A. Mangini (2010), Reconstruction of global ^{10}Be production over the past 250 ka from highly accumulating Atlantic drift sediments, *Quat. Sci. Rev.*, *29*(19–20), 2663–2672, doi:10.1016/j.quascirev.2010.06.017.

Creer, K. M., P. Readman, and A. M. Jacobs (1980), Palaeomagnetic and paleontological dating of a section at Gioia Tauro, Italy: Identification of the Blake event, *Earth Planet. Sci. Lett.*, *50*, 289–300.

Demory, F., N. R. Nowaczyk, A. Witt, and H. Oberhänsli (2005), High-resolution magnetostratigraphy of late Quaternary sediments from Lake Baikal, Siberia: Timing of intracontinental paleoclimatic responses, *Global Planet. Change*, *46*, 167–186.

Denham, C. R. (1976), Blake polarity episode in two cores from the Greater Antilles outer ridge, *Earth Planet. Sci. Lett.*, *29*, 422–443.

Dunai, T. J., and N. A. Lifton (2014), The nuts and bolts of cosmogenic nuclide production, *Elements*, *10*(5), 347–350, doi:10.2113/gselements.10.5.347.

Elsasser, W., E. P. Ney, and J. R. Winckler (1956), Cosmic-ray intensity and geomagnetism, *Nature*, *178*, 1226–1227.
Frank, M., B. Schwarz, S. Baumann, P. W. Kubik, M. Suter, and A. Mangini (1997), A 200 kyr record of cosmogenic radionuclide production rate and geomagnetic field intensity from ^{10}Be in globally stacked deep-sea sediments, *Earth Planet. Sci. Lett.*, *149*(1–4), 121–129.
Gallet, Y., M. D'Andrea, A. Genevey, F. Pinnock, M. Le Goff, and P. Matthiae (2014), Archaeomagnetism at Ebla (Tell Mardikh, Syria). New data on geomagnetic field intensity variations in the Near East during the Bronze Age, *J. Archaeol. Sci.*, *42*, 295–304, doi:10.1016/j.jas.2013.11.007.
Gee, J. S., S. Cande, J. Hildebrand, K. Donnelly, and R. Parker (2000), Geomagnetic intensity variations over the past 780 kyr obtained from near-seafloor magnetic anomalies, *Nature*, *408*, 827–832.
Genevey, A., Y. Gallet, and J.-C. Margueron (2003), Eight thousand years of geomagnetic field intensity variations in the eastern Mediterranean, *J. Geophys. Res.*, *108*(B5), 2228, doi:10.1029/2001JB001612.
Gubbins, D. (1999), The distinction between geomagnetic excursions and reversals, *Geophys. J. Int.*, *137*, F1–F3.
Guyodo, Y., and J.-P. Valet (1996), Relative variations in geomagnetic intensity from sedimentary records: The past 200,000 years, *Earth Planet. Sci. Lett.*, *143*, 23–36.
Guyodo, Y., and J.-P. Valet (1999), Global changes in intensity of the Earth's magnetic field during the past 800 kyr, *Nature*, *399*, 249–252.
Heikkilä, U., J. Beer, and J. Feichter (2009), Meridional transport and deposition of atmospheric ^{10}Be, *Atmos. Chem. Phys.*, *9*, 515–527.
Heikkilä, U., J. Beer, J. A. Abreu, and F. Steinhilber (2013), On the atmospheric transport and deposition of the cosmogenic radionuclides (^{10}Be): A review, *Space Sci. Rev.*, *176*(1–4), 321–332, doi:10.1007/s11214-011-9838-0.
Henken-Mellies, W. U., J. Beer, F. Heller, K. J. Hsü, C. Shen, G. Bonami, H. J. Hofmann, M. Suter, and W. Wölfli (1990), ^{10}Be and ^{9}Be in South Atlantic DSDP Site 519: Relation to geomagnetic reversals and to sediment composition, *Earth Planet. Sci. Lett.*, *98*, 267–276.
Herrero-Bervera, E., C. E. Helsley, A. M. Sarna-Wojcicki, K. R. Lajoie, C. E. Meyer, M. O. McWilliams, R. M. Negrini, B. D. Turrin, J. M. Donnelly-Nolan, and J.-C. Liddicoat (1994), Age and correlation of a paleomagnetic episode in the western united states by ^{40}Ar/^{39}Ar dating and tephrochronology: The Jamaica, Blake or a new polarity episode?, *J. Geophys. Res.*, *99*, 24,091–24,103, doi:10.1029/94JB01546.
Horiuchi, K., K. Kamata, S. Maejima, S. Sasaki, N. Sasaki, T. Yamazaki, S. Fujita, H. Motoyama, and H. Matsuzaki (2016), Multiple ^{10}Be records revealing the history of cosmic-ray variations across the Iceland Basin excursion, *Earth Planet. Sci. Lett.*, *440*, 105–114.
Hulot, G., C. C. Finlay, C. G. Constable, N. Olsen, and M. Mandea (2010), The Magnetic Field of Planet Earth, *Space Sci. Rev.*, *152*, 159–222, doi:10.1007/s11214-010-9644-0.
Jorry, S. J., A. W. Droxler, G. Mallarino, G. R. Dickens, S. J. Bentley, L. Beaufort, L. C. Peter- son, and B. N. Opdyke (2008), Bundled turbidite deposition in the central Pandora Trough (Gulf of Papua) since Last Glacial Maximum: Linking sediment nature and accumulation to sea level fluctuations at millennial timescale, *J. Geophys. Res.*, *113*, F01S19, doi:10.1029/2006JF000649.
Kawamura, K., et al. (2007), Northern Hemisphere forcing of climatic cycles in Antarctica over the past 360,000 years, *Nature*, *448*, 912–916, doi:10.1038/nature06015.
Knudsen, M. F., G. M. Henderson, M. Frank, C. Mac Niocaill, and P. W. Kubik (2008), In-phase anomalies in beryllium-10 production and palaeomagnetic field behaviour during the Iceland Basin geomagnetic excursion, *Earth Planet. Sci. Lett.*, *265*(3–4), 588–599, doi:10.1016/j.epsl.2007.10.051.
Korschinek, G., et al. (2010), A new value for the half-life of ^{10}Be by Heavy-Ion Elastic Recoil Detection and liquid scintillation counting, *Nucl. Instrum. Methods Phys. Res. B.*, *268*(2), 187–191, doi:10.1016/j.nimb.2009.09.020.
Korte, M., C. Constable, F. Donadini, and R. Holme (2011), Reconstructing the Holocene geomagnetic field, *Earth Planet. Sci. Lett.*, *312*, 497–505.
Kovaltsov, G. A., and I. G. Usoskin (2010), A new 3D numerical model of cosmogenic nuclide 10Be production in the atmosphere, *Earth Planet. Sci. Lett.*, *291*(1–4), 182–188, doi:10.1016/j.epsl.2010.01.011.
Laj, C., and J. E. T. Channell (2015), Geomagnetic excursions, in *Treatise on Geophysics*, *Geomagnetism*, chap. 10, vol. 5, edited by M. Kono, pp. 373–416, Elsevier, Amsterdam.
Laj, C., C. Kissel, A. Mazaud, J. E. T. Channell, and J. Beer (2000), North Atlantic palaeointensity stack since 75 Ka (NAPIS-75) and the duration of the Laschamp event, *Philos. Trans. R. Soc. London*, *358*(1768), 1009–1025.
Laj, C., C. Kissel, and J. Beer (2004), *High Resolution Global Paleointensity Stack Since 75 kyrs (GLOPIS-75) Calibrated to Absolute Values, Timescales of the Geomagnetic Field*, *AGU Monogr.*, vol. 145, pp. 255–265, AGU, Washington, D. C.
Laj, C., C. Kissel, and A. P. Roberts (2006), Geomagnetic field behavior during the Icelandic basin and Laschamp geomagnetic excursions: A simple transitional field geometry?, *Geochem. Geophys. Geosyst.*, *7*, Q03004, doi:10.1029/2005GC001122.
Laj, C., H. Guillou, and C. Kissel (2014), Dynamics of the Earth magnetic field in the 10–75 kyr period comprising the Laschamp and Mono Lake excursions: New results from the French Chaîne des Puys in a global perspective, *Earth Planet. Sci. Lett.*, *387*, 184–197.
Lal, D. (1988), Theoretically expected variations in the terrestrial cosmic-ray production rates of isotopes, in *Solar–Terrestrial Relationships and the Earth Environment in the last Millennia*, edited by G. Cini Castagnoli, pp. 216–233, Soc. Italiana di Fisica, Bologna.
Lal, D., and B. Peters (1967), Cosmic ray produced radioactivity on the Earth, in *Handbuch der Physik*, vol. XLVI/2, pp. 551–612, Springer, New York.
Landais, A., J. P. Steffensen, N. Caillon, J. Jouzel, V. Masson-Delmotte, and J. Schwander (2004), Evidence for stratigraphic distortion in the Greenland Ice Core Project (GRIP) ice core during Event 5e1 (120 kyr BP) from gas isotopes, *J. Geophys. Res.*, *109*, D06103, doi:10.1029/2003JD004193.
Langereis, C. G., M. J. Dekkers, G. J. DeLange, M. Paterne, and P. J. M. Santvoort (1997), Magnetostratigraphy and astronomical calibration of the last 1.1 Myr from an eastern Mediterranean piston core and dating of short events in the Brunhes, *Geophys. J. Int.*, *129*, 75–94.
Lanphere, M. A. (2000), Comparison of conventional K/Ar and ^{40}Ar/^{39}Ar dating of young mafic volcanic rocks, *Quat. Res.*, *53*, 294–301.
Liddicoat, J. C., and R. S. Coe (1979), Mono lake geomagnetic excursion, *J. Geophys. Res.*, *84*, 261–271, doi:10.1029/JB084iB01p00261.
Lisiecki, L. E., and M. E. Raymo (2005), A Pliocene–Pleistocene stack of 57 globally distributed benthic δ^{18}O record, *Paleoceanography*, *20*, PA1003, doi:10.1029/2004PA001071.
Liu, X. M., T. S. Liu, C. Liu, and M. Y. Chen (1988), The Chinese loess in Xifeng, I, The preliminary study on magnetostratigraphy of a loess profile in Xifeng area, Gansu Province, *Geophys. J. Int.*, *92*, 345–348.
Lund, S. P., J. S. Stoner, J. E. T. Channell, and G. Acton (2006), A summary of the paleomagnetic field variability recorded in Ocean Drilling Program Cores, *Phys. Earth Planet. Int.*, *156*, 194–204.
Lund, S. P., G. D. Acton, B. Clement, M. Okada, and T. Williams (2001), Brunhes chron magnetic field excursions recovered from Leg 172 sediments, in *Proceedings of the ODP Science Research*, vol. 172, edited by L. D. Keigwin et al., pp. 1–18, Tex. A&M Univ., Ocean Drilling Program.
Masarik, J., and J. Beer (1999), Simulation of particle fluxes and cosmogenic nuclide production in the Earth's atmosphere, *J. Geophys. Res.*, *104*, 12,099–12,111, doi:10.1029/1998JD200091.

Masarik, J., and J. Beer (2009), An updated simulation of particle fluxes and cosmogenic nuclide production in the Earth's atmosphere, *J. Geophys. Res.*, *114*, D11103, doi:10.1029/2008JD010557.

McFadden, M. A., L. C. Peterson, S. J. Bentley, G. R. Dickens, A. W. Droxler, and B. Opdyke (2006), Role of paleoclimate and paleoceanography in sediment delivery to the Gulf of Papua over the last 300 kyrs based on foraminiferal and organic matter stable isotope records, in *Annual Meeting*, Am. Assoc. of Petrol Geol., Houston, Tex.

McWilliams, M. (2001), Global correlation of the 223 ka Pringle Falls Event, *Int. Geol. Rev.*, *43*, 191–195.

Ménabréaz, L., N. Thouveny, D. L. Bourlès, P. Deschamps, B. Hamelin, and F. Demory (2011), The Laschamp geomagnetic dipole low expressed as a cosmogenic ^{10}Be atmospheric overproduction at ~41 ka, *Earth Planet. Sci. Lett.*, *312*(3–4), 305–317, doi:10.1016/j.epsl.2011.10.037.

Ménabréaz, L., D. L. Bourlès, and N. Thouveny (2012), Amplitude and timing of the Laschamp geomagnetic dipole low from the global atmospheric ^{10}Be overproduction: Contribution of authigenic ^{10}Be/^{9}Be ratios in west equatorial Pacific sediments, *J. Geophys. Res.*, *117*, B11101, doi:10.1029/2012JB009256.

Ménabréaz, L., N. Thouveny, D. L. Bourlès, and L. Vidal (2014), The geomagnetic dipole moment variation between 250 and 800 ka BP reconstructed from the authigenic ^{10}Be/^{9}Be signature in West Equatorial Pacific sediments, *Earth Planet. Sci. Lett.*, *385*, 190–205, doi:10.1016/j.epsl.2013.10.037.

Muscheler, R., J. Beer, P. W. Kubik, and H. A. Synal (2005), Geomagnetic field intensity during the last 60,000 years based on ^{10}Be and ^{36}Cl from the Summit ice cores and ^{14}C, *Quat. Sci. Rev.*, *24*(16–17), 1849–1860, doi:10.1016/j.quascirev.2005.01.012.

Nishiizumi, K., M. Imamura, M. W. Caffee, J. R. Southon, R. C. Finkel, and J. McAninch (2007), Absolute calibration of ^{10}Be AMS standards, *Nucl. Instrum. Methods Phys. Res. Section B*, *258*, 403–413.

Nowaczyk, N. R., and T. W. Frederichs (1999), Geomagnetic events and relative paleointensity variations during the past 300 ka recorded in Kolbeinsey ridge sediments, Iceland sea: Indication for a strongly variable geomagnetic field, *Int. J. Earth Sci.*, *88*, 116–131.

Nowaczyk, N. R., and J. Knies (2000), Magnetostratigraphic results from the eastern Arctic ocean: AMS 14C ages and relative paleointensity data of the Mono Lake and Laschamp geomagnetic reversal excursions, *Geophys. J. Int.*, *140*, 185–197.

Nowaczyk, N. R., T. W. Frederichs, A. Eisenhauer, and G. Gard (1994), Magnetostratigraphic data from late Quaternary sediments from the Yermak plateau, Arctic Ocean: Evidence for four geomagnetic polarity events within the last 170 ka of the Brunhes Chron, *Geophys. J. Int.*, *117*, 453–471.

Nowaczyk, N. R., U. Frank, J. Kind, and H. W. Arz (2013), A high-resolution paleointensity stack of the past 14 to 68 ka from Black Sea sediments, *Earth Planet. Sci. Lett.*, *384*, 1–16.

Oda, H., K. Nakamura, K. Ikehara, T. Nakano, M. Nishimura, and O. Khlystov (2002), Paleomagnetic record from Academician ridge, Lake Baikal: A reversal excursion at the base of marine oxygen isotope stage 6, *Earth Planet. Sci. Lett.*, *202*, 117–132.

Olson, P. I., R. S. Coe, P. E. Driscoll, G. A. Glatzmaier, and P. H. Roberts (2010), Geodynamo reversal frequency and heterogeneous core-mantle boundary heat flow, *Phys. Earth Planet. Int.*, *180*, 66–79.

Osete, M. L., J. Martin-Chivelet, C. Rossi, L. Edwards, R. Egli, M. B. Munoz-Garcia, X. Wang, F. J. Pavon-Carrasco, and F. Heller (2012), The Blake geomagnetic excursion recorded in a radiometrically dated speleothem, *Earth Planet. Sci. Lett.*, *353*, 173–181, doi:10.1016/j.epsl.2012.07.041.

Peate, D. W., J. H. Chen, G. J. Wasserburg, D. A. Papanastassiou, and J. W. Geissman (1996), ^{238}U-^{230}Th dating of a geomagnetic excursion in Quaternary basalts of the Albuquerque Volcanoes Field, New Mexico (USA), *Geophys. Res. Lett.*, *23*, 2271–2274, doi:10.1029/96GL02064.

Quidelleur, X., P. Y. Gillot, J. Carlut, and V. Courtillot (1999), Link between excursions and paleointensity inferred from abnormal field direction recorded at La Palma around 600 ka, *Earth Planet. Sci. Lett.*, *168*, 233–242.

Raisbeck, G. M., F. Yiou, M. Fruneau, J. M. Loiseaux, M. Lieuvin, and J. C. Ravel (1981), Cosmogenic ^{10}Be/^{7}Be as a probe of atmospheric transport processes, *Geophys. Res. Lett.*, *8*, 1015–1018, doi:10.1029/GL008i009p01015.

Raisbeck, G. M., F. Yiou, D. Bourlès, and D. V. Kent (1985), Evidence for an increase in cosmogenic ^{10}Be during a geomagnetic reversal, *Nature*, *315*, 315–317, doi:10.1038/315315a0.

Raisbeck, G. M., F. Yiou, O. Cattani, and J. Jouzel (2006), ^{10}Be evidence for the Matuyama-Brunhes geomagnetic reversal in the EPICA Dome C ice core, *Nature*, *444*(7115), 82–84, doi:10.1038/nature05266.

Raisbeck, G. M., F. Yiou, J. Jouzel, and T. F. Stocker (2007), Direct north-south synchronization of abrupt climate change record in ice cores using Beryllium 10, *Clim. Past*, *3*, 541–547.

Regoli, F., T. de Garidel-Thoron, K. Tachikawa, Z. Jian, L. Ye, A. W. Droxler, G. Lenoir, M. Crucifix, N. Barbarin, and L. Beaufort (2015), Progressive shoaling of the equatorial Pacific thermocline over the last eight glacial periods, *Paleoceanography*, *30*, 439–455, doi:10.1002/2014PA002696.

Reimer, P. J., et al. (2013), IntCal13 and Marine13 radiocarbon age calibration curves 0–50,000 years cal BP, *Radiocarbon*, *55*(4), 1869–1887, doi:10.2458/azu_js_rc.55.16947.

Roberts, A. P., L. Tauxe, and D. Heslop (2013), Magnetic paleointensity stratigraphy and high-resolution Quaternary geochronology: Successes and future challenges, *Quat. Sci. Rev.*, *61*, 1–16.

Robinson, C., G. M. Raisbeck, F. Yiou, B. Lehman, and C. Laj (1995), The relationship between ^{10}Be and geomagnetic field strength records in central North Atlantic sediments during the last 80 ka, *Earth Planet. Sci. Lett.*, *136*(3), 551–557, doi:10.1016/0012-821X(95)00202-N.

Shane, P., T. Black, and J. Westgate (1994), Isothermal plateau fission-track age for a paleomagnetic excursion in the Mamaku Ignimbrite, New-Zealand, and implications for late Quaternary stratigraphy, *Geophys. Res. Lett.*, *21*, 1695–1698, doi:10.1029/94GL01576.

Simon, Q., G. St-Onge, and C. Hillaire-Marcel (2012), Late Quaternary chronostratigraphic framework of deep Baffin Bay glaciomarine sediments from high-resolution paleo-magnetic data, *Geochem. Geophys. Geosyst.*, *13*, Q0AO03, doi:10.1029/2012GC004272.

Simon, Q., N. Thouveny, D. L. Bourlès, L. Nuttin, C. Hillaire-Marcel, and G. St-Onge (2016), Authigenic ^{10}Be/^{9}Be ratios and ^{10}Be-fluxes (^{230}Thxs-normalized) in central Baffin Bay sediments during the last glacial cycle: Paleoenvironmental implications, *Quat. Sci. Rev.*, *140*, 142–162, doi:10.1016/j.quascirev.2016.03.027.

Singer, B. S., M. K. Relle, K. A. Hoffman, A. Battle, H. Guillou, and J. C. Carracedo (2002), Ar/Ar ages from transitionally magnetized lavas on La Palma, Canary Islands and the geomagnetic instability timescale, *J. Geophys. Res.*, *107*(B11), 2307, doi:10.1029/2001JB001613.

Singer, B. S., K. A. Hoffman, R. S. Coe, L. L. Brown, B. R. Jicha, M. S. Pringle, and A. Chauvin (2005), Structural and temporal requirements for geomagnetic field reversal deduced from lava flows, *Nature*, *434*, 633–636.

Singer, B. S., K. A. Hoffman, E. Schnepp, and H. Guillou (2008a), Multiple Brunhes Chron excursions recorded in the West Eifel (Germany) volcanics: Support for long-held mantle control over the non-axial dipole field, *Phys. Earth Planet. Int.*, *169*, 28–40.

Singer, B. S., B. R. Jicha, B. T. Kirby, J. W. Geissman, and E. Herrero-Bervera (2008b), ^{40}Ar/^{39}Ar dating links Albuquerque volcanoes to the Pringle falls excursion and the geomagnetic instability time Scale, *Earth Planet. Sci. Lett.*, *267*(3–4), 584–595, doi:10.1016/j.epsl.2007.12.

Singer, B. S., H. Guillou, B. R. Jicha, E. Zanella, and P. Camps (2014), Refining the Quaternary Geomagnetic Instability Time Scale (GITS): Lava flow recordings of the Blake and Post-Blake excursions, *Quat. Geochronol.*, *21*, 16–28.

Smith, J. D., and J. H. Foster (1969), Geomagnetic reversal in the Brunhes normal polarity epoch, *Science*, *163*, 565–567.
Stoner, J. S., C. Laj, J. E. T. Channell, and C. Kissel (2002), South Atlantic and North Atlantic geomagnetic paleointensity stacks (0–80 ka): Implications for inter-hemispheric correlation, *Quat. Sci. Rev.*, *21*, 1141–1151.
Stoner J. S., J. E. T. Channell, D. A. Hodell, and C. Charles (2003), A 580 kyr paleomagnetic record from the sub-Antarctic south Atlantic (ODP Site 1089), *J. Geophys. Res.*, *108*(B5), 2244, doi:10.1029/2001JB001390.
Suganuma, Y., Y. Yokoyama, T. Yamazaki, K. Kawamura, C.-S. Horn, and H. Matsuzaki (2010), ^{10}Be evidence for delayed acquisition of remanent magnetization in marine sediments: Implication for a new age for the Matuyama–Brunhes boundary, *Earth Planet. Sci. Lett.*, *296*, 443–450.
Svensson, A., et al. (2008), A 60,000 year Greenland stratigraphic ice core chronology, *Clim. Past*, *4*, 47–57.
Tachikawa, K., O. Cartapanis, L. Vidal, L. Beaufort, T. Barlyaeva, and E. Bard (2011), The precession phase of hydrological variability in the Western Pacific Warm Pool during the past 400 ka, *Quat. Sci. Rev.*, *30*, 3716–3727.
Tachikawa, K., A. Timmermann, L. Vidal, C. Sonzogni, and O. E. Timm (2014), CO_2 radiative forcing and Intertropical Convergence Zone influences on western Pacific warm pool climate over the past 400 ka, *Quat. Sci. Rev.*, *86*(C), 24–34, doi:10.1016/j.quascirev.
Tauxe, L. (1993), Sedimentary records of relative paleointensity of the geomagnetic field: Theory and practice, *Rev. Geophys.*, *31*, 319–354, doi:10.1029/93RG01771.
Tauxe, L., J. L. Steindorf, and A. Harris (2006), Depositional remanent magnetization: Toward an improved theoretical and experimental foundation, *Earth Planet. Sci. Lett.*, *244*, 515–529.
Thouveny, N., K. M. Creer, and I. Blunk (1990), Extension of the Lac du Bouchet palaeomagnetic record over the last 120,000 years, *Earth Planet. Sci. Lett.*, *97*, 140–161.
Thouveny, N., J. Carcaillet, E. Moreno, G. Leduc, and D. Nérini (2004), Geomagnetic moment variation and paleomagnetic excursions since 400 kyr BP: A stacked record from sedimentary sequences of the Portuguese margin, *Earth Planet. Sci. Lett.*, *219*, 377–396.
Thouveny, N., D. L. Bourlès, G. Saracco, J. T. Carcaillet, and F. Bassinot (2008), Paleoclimatic context of geomagnetic dipole lows and excursions in the Brunhes, clue for an orbital influence on the geodynamo?, *Earth Planet. Sci. Lett.*, *275*(3–4), 269–284, doi:10.1016/j.epsl.2008.08.020.
Tison, J.-L., et al. (2015), Retrieving the paleoclimatic signal from the deeper part of the EPICA Dome C ice core, *Cryosphere*, *9*, 1633–1648, doi:10.5194/tc-9-1633-2015.
Tric, E., C. Laj, J.-P. Valet, P. Tucholka, M. Paterne, and F. Guichard (1991), The Blake geomagnetic event: Transition geometry, dynamical characteristics and geomagnetic significance, *Earth Planet. Sci. Lett.*, *102*, 1–13.
Tucholka, P., M. Fontugne, F. Guichard, and M. Paterne (1987), The Blake polarity episode in cores from the Mediterranean Sea, *Earth Planet. Sci. Lett.*, *86*, 320–326.
Valet, J.-P. (2003), Time variations in geomagnetic intensity, *Rev. Geophys.*, *41*(1), 1004, doi:10.1029/2001RG000104.
Valet, J.-P., and A. Fournier (2016), Deciphering records of geomagnetic reversals, *Rev. Geophys.*, *54*, 410–446, doi:10.1002/2015RG000506.
Valet, J.-P., and L. Meynadier (1993), Geomagnetic field intensity and reversals during the last four million years, *Nature*, *366*, 234–238.
Valet, J.-P., L. Meynadier, and Y. Guyodo (2005), Geomagnetic field strength and reversal rate over the past 2 million years, *Nature*, *435*, 802–805.
Valet, J.-P., F. Bassinot, A. Bouilloux, D. L. Bourlès, S. Nomade, V. Guillou, F. Lopes, N. Thouveny, and F. Dewilde (2014), Geomagnetic, cosmogenic and climatic changes across the last geomagnetic reversal from Equatorial Indian Ocean sediments, *Earth Planet. Sci. Lett.*, *397*, 67–79, doi:10.1016/j.epsl.2014.03.053.
Vanyo, J., P. Wilde, P. Cardin, and P. Olson (1995), Experiments on precessing flows in the Earth's liquid core, *Geophys. J. Int.*, *121*(1), 136–142, doi:10.1111/j.1365-246X.1995.tb03516.x.
Vogt, S., G. F. Herzog, and R. C. Reedy (1990), Cosmogenic nuclides in extraterrestrial materials, *Rev. Geophys.*, *28*(3), 253–275, doi:10.1029/RG028i003p00253.
Wagner, G., J. Masarik, J. Beer, S. Baumgartner, D. Imboden, P. W. Kubik, H. A. Synal, and M. Suter (2000), Reconstruction of the geomagnetic field between 20 and 60 kyr BP from cosmogenic radionuclides in the GRIP ice core, *Nucl. Instrum. Methods Phys. Res. B*, *172*, 597–604.
Xuan, C., J. E. T. Channell, and D. A. Hodell (2016), Quaternary magnetic and oxygen isotope stratigraphy in diatom-rich sediments of the southern Gardar Drift (IODP Site U1304, North Atlantic), *Quat. Sci. Rev.*, *142*, 74–89.
Yamazaki, T., and H. Oda (2002), Orbital influence on Earth's magnetic field: 100,000-year periodicity in inclination, *Science*, *295*, 2435–2438.
Yamazaki, T., and N. Yoka (1994), Long-term secular variation of the geomagnetic field during the last 200 kyr recorded in sediment cores from the western equatorial Pacific, *Earth Planet. Sci. Lett.*, *128*, 527–544.
Yiou, F., G. M. Raisbeck, D. L. Bourlès, C. Lorius, and N. I. Barkov (1985), ^{10}Be in ice at Vostok Antarctica during the last climatic cycle, *Nature*, *316*(6029), 616–617.
Zhang, K., and D. Gubbins (2000), Is the geodynamo process intrinsically unstable?, *Geophys. J. Int.*, *140*, F1–F4.
Ziegler, L. B., C. G. Constable, C. L. Johnson, and L. Tauxe (2011), PADM2M: a penalized maximum likelihood model of the 0–2 Ma palaeomagnetic axial dipole moment, *Geophys. J. Int.*, *184*, 1069–1089, doi:10.1111/j.1365-246X.2010.04905.x.